

Inference of Internal Stress in a Cell Monolayer

V. Nier¹, S. Jain², C. T. Lim^{2,3}, S. Ishihara⁴, B. Ladoux^{2,5} and P. Marcq^{1,*}

1 Sorbonne Universités, UPMC Univ Paris 6, Institut Curie, CNRS, UMR 168, Laboratoire Physco-Chimie Curie, Paris, France

2 Mechanobiology Institute, National University of Singapore, Singapore

3 Department of Biomedical Engineering and Department of Mechanical Engineering, National University of Singapore, Singapore

4 Department of Physics, Meiji University, Kawasaki, Kanagawa, Japan

5 Institut Jacques Monod, CNRS UMR 7592 and Université Paris Diderot, Paris, France

* Corresponding Author philippe.marcq@curie.fr

Abstract

We combine traction force data with Bayesian inversion to obtain an absolute estimate of the internal stress field of a cell monolayer. The method, Bayesian inversion stress microscopy (BISM), is validated using numerical simulations performed in a wide range of conditions. It is robust to changes in each ingredient of the underlying statistical model. Importantly, its accuracy does not depend on the rheology of the tissue. We apply BISM to experimental traction force data measured in a narrow ring of cohesive epithelial cells, and check that the inferred stress field coincides with that obtained by direct spatial integration of the traction force data in this quasi-one-dimensional geometry.

1 Introduction

Dynamical behaviors of multicellular assemblies play a crucial role during tissue development [1] and in the maintenance of adult tissues [2]. In addition, dysregulation of multicellular structures may lead to pathological situations such as tumor formation and tumor progression [3]. In this context, cell monolayers have been extensively studied to model *in vivo* tissue functions. Such approaches allow for well-controlled experiments, which have been performed in a variety of settings, such as monolayer spreading [4, 5], wound healing [6, 7], channel flow [8, 9], confined flow [10, 11], collective migration [12, 13]. The dynamics of multicellular assemblies is regulated through mechanical forces that act upon cell adhesive structures. These forces are exerted at the cell-substrate interface [14], but also through cell-cell junctions [15]. The transmission of stresses within multicellular assemblies is thus important to understand collective movements, cell rearrangements and tissue homeostasis. Even though kinematic information is readily available, mechanical properties that rely on internal stress are less well understood. Indeed a number of important biological questions, such as the determination of the molecular mechanisms that underlie the transmission of force within a tissue [16], necessitate a measurement of internal stresses.

Several internal force measurement methods have been proposed and implemented (see [17] for a recent review): at the molecular scale, Förster resonance energy transfer [18, 19]; at the cell scale, microrheology [20, 21]; at the tissue scale, liquid drops [22], birefringence [23], or laser ablation [24, 25]. Although one would ideally like to read out from data the spatio-temporal dependence of the full stress field, the above methods yield either a local, sub-tissue scale measurement [18, 19, 20, 21, 22]; or a subset of the components of the stress tensor [23], or a relative measurement, up to an undetermined multiplicative constant [24, 25]. Monolayer stress microscopy (MSM), first introduced in [26], does not suffer from these drawbacks: it builds upon the measurement of traction force data to estimate the stress field of monolayers of cohesive cells. Indeed, the force exerted by cells on a planar deformable substrate can be computed from the displacement field of the underlying layer [27, 28], using either: *(i)* traction force microscopy [29, 30, 5] where small beads are inserted within the (elastic) substrate, their displacements are measured, and the traction forces are obtained by solving an inverse elastic problem; or *(ii)* arrays of micropillars [31, 32, 33], where the traction forces are simply proportional to the in-plane displacements of the pillars. However, once the traction forces are known, obtaining the internal stress from the force balance equations is an underdetermined problem since, in the two dimensional case, three components of the symmetrical stress tensor must be obtained from two traction force components. In MSM [26, 34], these equations become well-posed thanks to an additional hypothesis on tissue rheology: the cell monolayer is assumed to be a linear, isotropic elastic body. MSM has been validated independently on numerical data using particle dynamics simulations: in [35], the reasonable accuracy of stress reconstruction from data that does not correspond to an elastic rheology has been attributed to the weakness of shear stresses in both simulated and living tissues. Assuming again that the tissue is an elastic body, and in addition that the displacement field is continuous at the cell-substrate interface, internal stresses may also be computed directly from substrate displacement data, circumventing the need to compute traction forces [36].

In the presence of cell divisions and extrusions that constantly rearrange a tissue [37], it is not clear that its rheology is that of a solid body. To our knowledge, the elastic rheology hypothesis has not been directly validated, while alternative rheologies have been proposed in the literature [38, 39, 40, 7] and shown to model successfully specific aspects of the mechanical behaviour of cell monolayers. Further, the rheology of multicellular assemblies may depend on the timescale [37], as well as on the type of cell considered [41]. These caveats call for a method to accurately estimate the internal stress field of a cell monolayer irrespective of the underlying rheology.

A classical way to solve underdetermined inversion problems involves Bayesian inference [42], a technique originating in statistics [43], and now widely used in physics [44] and biophysics [45]. Of note, Bayesian inversion has also been used to solve the inverse elastic problem of traction force microscopy [46, 47]. Recently, some among us proposed a Bayesian force inference method based on cell geometry, and applied it to segmented images of the *Drosophila* pupal wing and notum [48, 49, 50]. The tissue-scale stress arises from coarse-graining of cell-cell interactions. For tight epithelia where adherens junctions are a key player of force transmission between neighboring cells, it is reasonable to as-

sume that the cell-scale contribution to stress is mostly related to local contact within the apical side of the epithelium, whereas basal contributions from, *e.g.* lamellipodia, are negligible. Accordingly, the dominant contributors to tissue-scale stress were identified as cell pressures and cell-cell junction tensions, and force balance equations were written at each cell vertex, resulting in an underdetermined system. This system was solved using Bayesian inversion [42], where the inferred tensions and pressures were the most likely values (the modes) of a posterior distribution function. In the case of the fruitfly pupal wing, it turned out that tissue stress, obtained by coarse-graining, is oriented by external forces, and that its anisotropy promotes hexagonal cell packing [49]. Similar systems of equations may become well-posed thanks to additional hypotheses (equal cell pressures [50, 51]), or when cell pressures are not required [52]. However the stress is measured up to an arbitrary additive constant: its absolute value is out of reach since the input data are cell vertex positions and cell junction angles.

Below, we formulate Bayesian inversion stress microscopy (BISM), a method to estimate the internal stress field of a cell monolayer from traction force microscopy measurements. Importantly, BISM yields an absolute measure of the stress and dispenses with hypotheses on monolayer rheology. We define BISM and introduce statistical measures of its accuracy. The method is first validated using numerical simulations that provide traction force data. The inferred stress field, once computed, is compared to the simulated stress data used as a reference. Robustness is checked by implementing changes in the statistical model, as well as in the mechanical ingredients of the numerical simulations. BISM is further validated using experimental data in a quasi-one-dimensional geometry that allows for a direct calculation of the stress field by spatial integration of the traction force field. Finally, our results are compared with existing methods.

2 Methods

2.1 Mechanics

Within a continuum description, a flat, thin cell monolayer is characterized at position \vec{r} and time t by a field of two-dimensional internal stresses $\sigma(\vec{r}, t)$ and by a field of external surfacic forces $\vec{t}(\vec{r}, t)$ that the monolayer exerts on the substrate. Since inertia is negligible, the balance of linear momentum reads in vector form

$$\text{div } \sigma = \vec{t}, \quad (1)$$

and in cartesian coordinates (x, y) (see *Supplementary Text 1.2* for polar coordinates)

$$\frac{\partial \sigma_{xx}}{\partial x} + \frac{\partial \sigma_{xy}}{\partial y} = t_x \quad (2)$$

$$\frac{\partial \sigma_{yx}}{\partial x} + \frac{\partial \sigma_{yy}}{\partial y} = t_y \quad (3)$$

Note that at this stage, due to the grid definition (see below and Fig. 1b), we do not enforce the symmetry of the stress tensor (equality of the shear stress components due

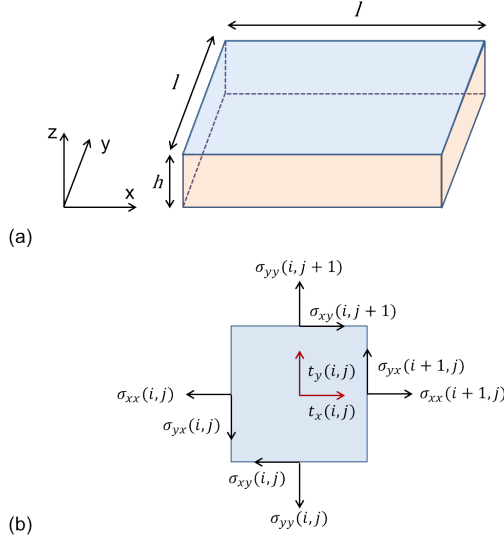


Figure 1: **Discrete monolayer mechanics.** (a) A tissue element of volume $l^2 \times h$. (b) Pictorial representation of local force balance, Eqs. (5,6), see text for definitions. To see this figure in color, go online.

to angular momentum conservation [53]). With a confined monolayer in mind [10, 11], the boundary condition reads

$$\sigma_{ij} n_j = 0 \quad (4)$$

where \vec{n} denotes the vector normal to the edge, and summation over repeated indices is implied. In the plane, the units of stresses and (surfacic) forces are Pa.m and Pa respectively. Assuming that the monolayer height is uniform and constant $h(\vec{r}, t) = h_0$, the 3D stress reads $\sigma_{3D} = \sigma/h_0$. When spatial or temporal variations of the height cannot be neglected [4, 5], BISM can be implemented by replacing $\vec{t}(\vec{r}, t)$ by $\vec{t}(\vec{r}, t)/h(\vec{r}, t)$ and by inferring the 3D stress from $\text{div } \sigma_{3D} = \vec{t}/h$, provided that the height remains small compared to the system size, as is generally the case for *in vitro* cell monolayers [26, 54]. A treatment of the full 3D case where the height is comparable or larger than the system size is beyond the scope of this work.

Since experimental traction forces are measured with a finite spatial resolution l , assumed to be isotropic for simplicity, we write a force balance equation in each of a large number of square surface elements of area l^2 (see Fig. 1a). We aim at inferring the stress tensor $\sigma(i, j) = \begin{pmatrix} \sigma_{xx}(i, j) & \sigma_{yx}(i, j) \\ \sigma_{xy}(i, j) & \sigma_{yy}(i, j) \end{pmatrix}$ in each element. The traction force exerted by the tissue in element (i, j) on the substrate is $\vec{t}(i, j)$, with components $t_x(i, j), t_y(i, j)$. In the case of a rectangular grid with C columns and R rows, the discretized force balance equation for element (i, j) reads

$$l [\sigma_{xx}(i+1, j) - \sigma_{xx}(i, j) + \sigma_{xy}(i, j+1) - \sigma_{xy}(i, j)] = l^2 t_x(i, j) \quad (5)$$

$$l [\sigma_{yx}(i+1, j) - \sigma_{yx}(i, j) + \sigma_{yy}(i, j+1) - \sigma_{yy}(i, j)] = l^2 t_y(i, j) \quad (6)$$

to lowest order in l (see Fig. 1b). We thus have $N = C \times R$ variables for t_x and t_y , $(C+1) \times R$ variables for σ_{xx} and σ_{yx} and $C \times (R+1)$ variables for σ_{yy} and σ_{xy} . Defining traction force and stress *vectors* as

$$\begin{aligned}\vec{T} &= [t_x(1,1) \cdots t_x(R,C) t_y(1,1) \cdots t_y(R,C)]^t \\ \vec{\sigma} &= [\sigma_{xx}(1,1) \cdots \sigma_{xx}(C+1,R) \sigma_{yy}(1,1) \cdots \sigma_{yy}(C,R+1) \\ &\quad \sigma_{xy}(1,1) \cdots \sigma_{xy}(C,R+1) \sigma_{yx}(1,1) \cdots \sigma_{yx}(C+1,R)]^t\end{aligned}$$

where the superscript t denotes the transpose, we rewrite Eqs. (5-6) in matrix form

$$A\vec{\sigma} = \vec{T}. \quad (7)$$

The matrix A , of size $2N \times (4N + 2(C+R))$, may be decomposed as

$$A = \begin{pmatrix} A_x & 0 & A_y & 0 \\ 0 & A_y & 0 & A_x \end{pmatrix} \quad (8)$$

where A_x and A_y correspond to the discretized matrix forms, at second order in l , of the partial derivatives with respect to x and y .

2.2 Statistics

To solve the underdetermined linear system (7), we implement Bayesian inversion [42]: all variables and parameters of the problem are probabilized. For simplicity, we use wherever possible Gaussian probability distribution functions, denoted $\mathcal{N}(\vec{X} | \vec{m}, S)$ for a multivariate (vector) Gaussian random variable \vec{X} with mean \vec{m} and covariance matrix S .

Likelihood The first ingredient of the statistical model is the likelihood function $L(\vec{T} | \vec{\sigma})$, which contains information provided by experimental measurements. For experimental data, the force balance equations (7) are verified up to an additive noise due to measurement errors. Assuming this noise to be Gaussian with zero mean and uniform covariance matrix $S = s^2 I$, where the parameter s^2 denotes the noise variance and I is the identity matrix, the likelihood is expressed as $L(\vec{T} | \vec{\sigma}) = \mathcal{N}(\vec{T} | A\vec{\sigma}, s^2 I)$ or

$$L(\vec{T} | \vec{\sigma}) = \left(\frac{1}{\sqrt{2\pi s^2}} \right)^{2N} \exp \left[-\frac{\|\vec{T} - A\vec{\sigma}\|^2}{2s^2} \right] \quad (9)$$

where $\|\dots\|$ is the (L_2) Euclidean norm.

Prior Second, the prior probability distribution function $\pi(\vec{\sigma})$ embeds additional information concerning the stress field:

- (i) we assume that the stress obeys a Gaussian distribution function with zero mean $\vec{\sigma}_0 = \vec{0}$ and covariance matrix $s_0^2 I$;

- (ii) we enforce the equality of the two off-diagonal components of the stress tensor: in compact vector form $\vec{\sigma}_{xy} = \vec{\sigma}_{yx}$, *i.e.* $\sigma_{xy}(i, j) + \sigma_{xy}(i, j + 1) = \sigma_{yx}(i, j) + \sigma_{yx}(i + 1, j) \quad \forall(i, j)$ (see Fig. 1b and *ST 1.3*);
- (iii) we enforce the boundary conditions (4), namely two conditions at each boundary element (i, j) , written in compact vector form $\vec{\sigma}_{BC} = \vec{0}$.

Up to a normalizing factor, the prior reads

$$\pi(\vec{\sigma}) \propto \exp \left[-\frac{\|\vec{\sigma}\|^2 + \alpha_{xy}^2 \|\vec{\sigma}_{xy} - \vec{\sigma}_{yx}\|^2 + \alpha_{BC}^2 \|\vec{\sigma}_{BC}\|^2}{2s_0^2} \right] \quad (10)$$

or

$$\pi(\vec{\sigma}) = \left(\frac{1}{\sqrt{2\pi|B|s_0^2}} \right)^{4N+2(R+C)} \exp \left[-\frac{\vec{\sigma}^t B^{-1} \vec{\sigma}}{2s_0^2} \right] \quad (11)$$

The second ingredient of the statistical model is a Gaussian prior $\pi(\vec{\sigma}) = \mathcal{N}(\vec{\sigma} \mid \vec{0}, S_0 = s_0^2 B)$ where B is a reduced covariance matrix of determinant $|B|$. Note that a Gaussian prior suppresses stress values larger than a few times s_0 (see [55] for a similar approach in the context of traction force microscopy). In practice, we set the hyperparameters α_{xy} and α_{BC} to the values $\alpha_{xy} = \alpha_{BC} = 10^3$, large enough for conditions (ii) and (iii) to be enforced (see *ST 3.2* for a discussion of these values). If required by a given experimental set-up, the boundary conditions should be modified appropriately in the definition of the prior.

Resolution According to Bayes' theorem, the posterior (conditional) probability distribution function $\Pi(\vec{\sigma} \mid \vec{T})$ of the stress given the traction force data is proportional to the product of the likelihood by the prior

$$\Pi(\vec{\sigma} \mid \vec{T}) \propto L(\vec{T} \mid \vec{\sigma}) \times \pi(\vec{\sigma}) \quad (12)$$

Since both are Gaussian, the posterior is also Gaussian $\Pi(\vec{\sigma} \mid \vec{T}) = \mathcal{N}(\vec{\sigma} \mid \vec{\sigma}_\Pi, S_\Pi)$, with a covariance matrix S_Π and a mean $\vec{\sigma}_\Pi$ given by [42]

$$S_\Pi = (S_0^{-1} + A^t S^{-1} A)^{-1} \quad (13)$$

$$\vec{\sigma}_\Pi = S_\Pi A^t S^{-1} \vec{T} \quad (14)$$

We use maximum a posteriori (MAP) estimation [42] and define the inferred stress $\vec{\hat{\sigma}}$ as the mode (maximal value) of the posterior $\vec{\hat{\sigma}} = \vec{\sigma}_\Pi$. Qualitatively, the underdeterminacy has been lifted: $4N + 2(R + C)$ unknown stress values are determined from $2N$ traction force values, $4N + 2(R + C)$ conditions from the Gaussian distribution of the stress tensor, N equalities of the two shear components and $4(R + C)$ boundary conditions.

In this Gaussian model, MAP estimation is identical to minimization of a Tikhonov potential [42]. The dimensionless regularization parameter

$$\Lambda = \frac{l^2 s^2}{s_0^2} \quad (15)$$

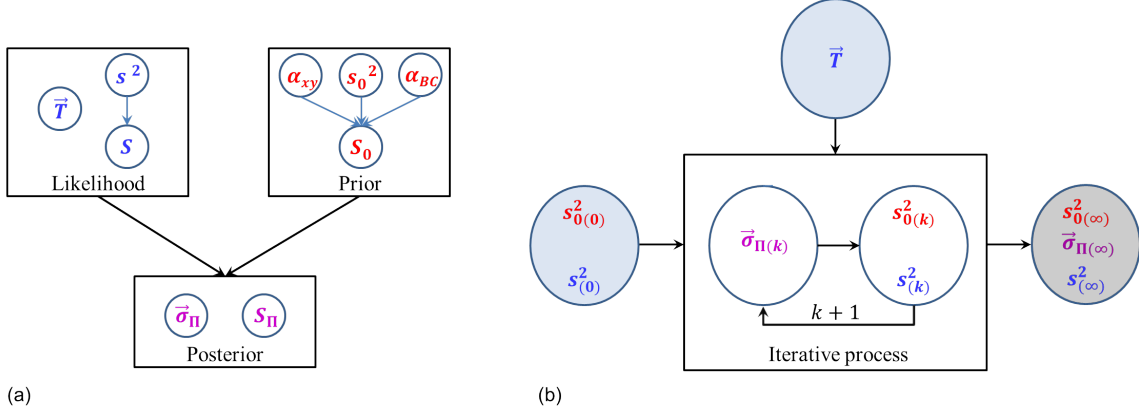


Figure 2: **Schematics of BISM.** To see this figure in color, go online. (a) Both the likelihood (with parameter s^2), and the prior (with hyperparameters s_0^2 , α_{xy} and α_{BC}) contribute to the definition of the posterior, a Gaussian distribution function of mean $\vec{\sigma}_\Pi$ and covariance matrix S_Π . Given numerical values of s^2 , s_0^2 , α_{xy} and α_{BC} , the MAP estimator of the stress $\vec{\sigma}$ is the mode of the posterior $\vec{\sigma}_\Pi$, Eq. (14). (b) In BISM, the values of s^2 and s_0^2 are not given *a priori*, but determined self-consistently within a hierarchical Bayesian construction. MAP estimation is performed iteratively, by successively optimizing the posterior for the mode $\vec{\sigma}_{(k)}$, Eqs. (13-14), and for the variances $s_{(k)}^2$, $s_{0(k)}^2$, Eqs. (19-20), until convergence to a fixed point is reached. The estimator of the stress $\vec{\sigma}$ is defined as the asymptotic value $\vec{\sigma}_{\Pi\infty}$, computed using $s_{(\infty)}^2 = \lim_{k \rightarrow \infty} s_{(k)}^2$ and $s_{0(\infty)}^2 = \lim_{k \rightarrow \infty} s_{0(k)}^2$ in Eqs. (13-14), with a regularization parameter $\Lambda_{(\infty)} = l^2 s_{(\infty)}^2 / s_{0(\infty)}^2$. A flowchart of the algorithm is given in Fig. S6 in the Supporting Material.

quantifies the relative weight given to the prior, compared to the likelihood, when performing Bayesian inversion. Factoring out $(sl)^2$, Eqs. (13-14) read

$$S_\Pi = (sl)^2 (\Lambda B^{-1} + l^2 A^t A)^{-1} \quad (16)$$

$$\vec{\sigma}_\Pi = (\Lambda B^{-1} + l^2 A^t A)^{-1} l^2 A^t \vec{T} \quad (17)$$

Since the product Al is dimensionless and independent of l , the posterior covariance (16) is a function of Λ and sl , while the posterior mode (17) depends upon Λ and $l\vec{T}$.

Hyperprior For generality sake, we probabilize the parameter s^2 and the hyperparameter s_0^2 , yet undetermined in Eqs. (13-14) (recall that $S = s^2 I$ and $S_0 = s_0^2 B$). Within the framework of hierarchical Bayesian descriptions, the model is closed by the *hyperprior* probability distribution functions $H(s^2)$ and $H(s_0^2)$ [56, 57]. Up to a normalizing factor,

the posterior now reads (see Fig. 2a)

$$\Pi(\vec{\sigma} | \vec{T}) \propto L(\vec{T} | \vec{\sigma}, s^2) \times \pi(\vec{\sigma} | s_0^2) \times H(s^2) \times H(s_0^2) \quad (18)$$

For simplicity, we use Jeffreys' non-informative hyperprior: $H(s^2) \propto 1/s^2$, $H(s_0^2) \propto 1/s_0^2$ [56, 57].

Simultaneous a posteriori optimization with respect to $\vec{\sigma}$, s^2 and s_0^2 being intractable, we solve the problem iteratively, starting from initial values $s_{(0)}^2$ and $s_{0(0)}^2$ (see Fig. 2b). At step $k \geq 1$, we first calculate the mode $\vec{\sigma}_{\Pi(k)}$ from previous values $s_{(k-1)}^2$, $s_{0(k-1)}^2$, Eqs. (13-14). Maximizing the posterior with respect to each hyperparameter yields the updated hyperparameter values

$$s_{(k)}^2 = \frac{1}{2N+2} \|\vec{T} - A\vec{\sigma}_{\Pi(k)}\|^2 \quad (19)$$

$$s_{0(k)}^2 = \frac{1}{4N+2(R+C)+2} \vec{\sigma}_{\Pi(k)}^t B^{-1} \vec{\sigma}_{\Pi(k)} \quad (20)$$

Once convergence is reached, $s_{(k)}^2 \rightarrow s_{(\infty)}^2$, $s_{0(k)}^2 \rightarrow s_{0(\infty)}^2$, the stress estimate is defined as $\vec{\sigma} = \vec{\sigma}_{\Pi(\infty)}$, computed from Eqs. (13-14) with the optimal values $s_{(\infty)}^2$ and $s_{0(\infty)}^2$. An estimate $\delta\vec{\sigma}$ of the error on $\vec{\sigma}$ is calculated as the square root of the diagonal values of the covariance matrix $S_{\Pi(\infty)}$. Since the marginal distribution of traction forces is Gaussian, with a covariance matrix $S_T = S + A S_0 A^t$ [42], we also calculate an estimate $\delta\vec{T}$ of the error on the traction force as the square root of the diagonal values of S_T .

2.3 Measures of accuracy

The numerical resolution of a set of hydrodynamical equations yields a numerical data set $\{t^{\text{num}}\}$ of traction forces, from which we compute a set $\{\sigma^{\text{inf}}\}$ of inferred stresses. Since the numerical data set $\{\sigma^{\text{num}}\}$ of stresses is also available, measures of accuracy involving numerical simulations typically compare $\{\sigma^{\text{inf}}\}$ with $\{\sigma^{\text{num}}\}$.

A classical ‘‘goodness-of-fit’’ measure is the coefficient of determination, defined for the σ_{xx} component of the stress as

$$R_{xx}^2 = 1 - \frac{\sum (\sigma_{xx}^{\text{num}} - \sigma_{xx}^{\text{inf}})^2}{\sum (\sigma_{xx}^{\text{num}} - \langle \sigma_{xx}^{\text{num}} \rangle)^2} \quad (21)$$

where the sums and the averages $\langle \dots \rangle$ are performed over space. Similar definitions apply to other components, and allow to define an aggregate coefficient of determination R_σ^2 averaged over all stress components. Accurate estimates correspond to numerical values of R_σ^2 close to 1. The discretized force balance equations (5-6), used as a definition of inferred traction forces, yield a set $\{t^{\text{inf}}\}$ of inferred traction forces computed from the set of inferred stresses $\{\sigma^{\text{inf}}\}$. Comparing $\{t^{\text{num}}\}$ with $\{t^{\text{inf}}\}$ allows to define similarly a R_T^2 diagnostic for numerical data.

When analyzing an experimental data set $\{t^{\text{exp}}\}$ of traction forces, R_σ^2 cannot be computed in the absence of a reference set of stresses. As above, comparing $\{t^{\text{exp}}\}$ with

$\{t^{\text{inf}}\}$ allows to define a measure of accuracy for experimental data, the coefficient of determination R_T^2 . An alternative measure of predictive accuracy is the χ_T^2 diagnostic, defined as the average value of the square of reduced residuals

$$\chi_T^2 = \frac{1}{2N} \sum \frac{(t^{\text{exp}} - t^{\text{inf}})^2}{\delta \hat{T}^2} \quad (22)$$

where the sum is performed over space and over traction force components. This measure of accuracy is, up to a normalizing factor, similar to the “omnibus goodness-of-fit” measure advocated in [56, 57]. The estimated standard deviation $\delta \hat{T}$ may be replaced in Eq. (22) by the measurement error δt . Numerical values of χ_T^2 close to 0 are indicators of high accuracy.

A last test of accuracy is provided by the calculation of average experimental stress values from traction force data [53], which may be compared with the average inferred stresses for each component (see Sec. 3.4 and *ST 1.4*).

2.4 Experimental methods

We used MDCK (Madin-Darby canine kidney) cells as an epithelial cell model.

Cell Culture MDCK wild-type cells were cultured in media containing DMEM (Life Technologies), 10 % FBS (Life Technologies) and 1 % antibiotics (penicillin and streptomycin).

Micro-contact printing and substrate preparation for Traction Force Microscopy We measured the traction forces exerted by cells on their substrate by using soft silicone gel as previously described [58]. Fluorescent beads were deposited onto the gel to measure the displacement field. Briefly, a thin layer of the gel was spread on a glass bottom dish and then cured at 80°C for 2 hours. Cured gel was silanized using 5% solution of (3-aminopropyl) triethoxysilane (APTES, Sigma) in pure ethanol. This gel was later incubated for 5 minutes with 100 nm carboxylated fluorescent beads (Invitrogen) suspended in deionized (DI) water. Subsequently, the substrate was dried and micro-contact printed with fibronectin [13, 59] using a thin water soluble Polyvinyl Alcohol (PVA) membrane which allows the transfer of fibronectin on soft gel. The PVA membrane was later dissolved and the non-contact printed areas were blocked using 0.2 % pluronics (Sigma) solution. The substrate was then washed and was seeded with cells. Cells were allowed to grow until the micro-contact printed area was fully covered.

The images were acquired using phase contrast and fluorescent channels to record cell positions and bead displacements, respectively.

For analysis, the imaging drifts were corrected in **ImageJ** (NIH) using the Image Stabilizer plugin [60]. To analyze the displacement field of beads, we used an open source iterative PIV (particle image velocimetry) plugin in **ImageJ** [61]. To reconstruct the traction force field from the obtained displacement field, an open source Fourier transform traction cytometry (FTTC) plugin was used in **ImageJ** [61]. The resulting traction force values were taken for the validation of the BISM inferred stress fields. To estimate

the experimental error δt_{exp} made on traction force measurements, we calculated the mean value of traction forces measured on square regions of the substrate devoid of cells (surface area $50 \times 50 \mu\text{m}^2$).

Monolayer height measurement The confluent cell monolayer was fixed for immunofluorescence microscopy. Actin present inside the cells was fluorescently labeled using Alexa Fluor 488-conjugated phalloidin (Invitrogen) at 1:1000 dilution in PBS. To measure tissue height, overall cell shape was then visualized with the help of cortical actin. Imaging was done using a Zeiss LSM 780 confocal microscope with a step size of $0.4 \mu\text{m}$ to capture the entire height of the tissue. In the confined ring shape geometry, height was measured at different locations to obtain the mean value and standard deviation of the monolayer height $h = 5.3 \pm 1.2 \mu\text{m}$.

3 Results

3.1 Validation: numerical data

A first example of the application of BISM to a numerical data set is given by using the traction force field of a compressible viscous fluid driven by active force dipoles, interacting with its substrate through an effective fluid friction force, and confined in a square, with the boundary conditions (4). We solve this problem on a $100 \times 100 \mu\text{m}^2$ square over a regular cartesian grid with $C = R = 50$, $N = C \times R = 2500$ and $l = 2 \mu\text{m}$ (see *ST 1.1*). We use material parameter values typical of cell monolayers: friction coefficient $\xi_v = 10^0 \text{ kPa } \mu\text{m}^{-1}\text{s}$ [7], shear viscosity $\eta = 10^3 \text{ kPa } \mu\text{m s}$ [62], and compression viscosity $\eta' = \eta$. To account for the measurement error, we add to the traction force field a white noise of relative amplitude 5% (variance $s_{\text{exp}}^2 = 1.2 \cdot 10^{-3} \text{ kPa}^2$), and obtain the numerical data set $\{t^{\text{num}}\}$ of traction forces (Fig. 3a), referred to below as *Viscous*. We checked that the total sum of the traction forces is close to zero, as expected for a closed system with negligible inertia.

Bayesian inversion is performed with a custom-made script written in **Matlab** (The MathWorks, Inc.). With $s_{(0)}^2 = 10^{-1} \text{ kPa}^2$ and $s_{0(0)}^2 = 10^2 \text{ kPa}^2 \mu\text{m}^2$ as initial values, the resolution method converges in a few steps towards the asymptotic hyperparameter values $s_{(\infty)}^2 = 4.7 \cdot 10^{-7} \text{ kPa}^2$ and $s_{0(\infty)}^2 = 3.4 \cdot 10^{-1} \text{ kPa}^2 \mu\text{m}^2$, or $\Lambda_{(\infty)} = 5.5 \cdot 10^{-6}$ (see *ST 3.1* and Fig. S4a in the Supporting Material) The data sets $\{\sigma^{\text{num}}\}$ and $\{\sigma^{\text{inf}}\}$ of simulated and inferred stresses are shown in Fig. 3b-c: we find that their spatial structures are quite similar. This observation is confirmed quantitatively by plotting component by component the inferred stress *vs.* the simulated stress (Figs. 3d-f), and by the numerical values of the coefficients of determination $R_{xx}^2 = 0.94$, $R_{yy}^2 = 0.97$, $R_{xy}^2 = 0.95$, yielding an aggregate measure of accuracy $R_{\sigma}^2 = 0.96$, close to 1. Using the inferred data set $\{t^{\text{inf}}\}$ of traction forces, we also obtain $1 - R_T^2 = 2 \cdot 10^{-5}$ and $\chi_T^2 = 7 \cdot 10^{-7}$, indicating that all the information contained in the traction force data is used. An order of magnitude of the error bar is given by the standard deviations, calculated using (16): $\delta\hat{\sigma} \approx 10^2 l s_{(\infty)} \approx 10^{-1} \text{ kPa } \mu\text{m}$, corresponding to $\approx 10 \%$ of the maximal stresses.

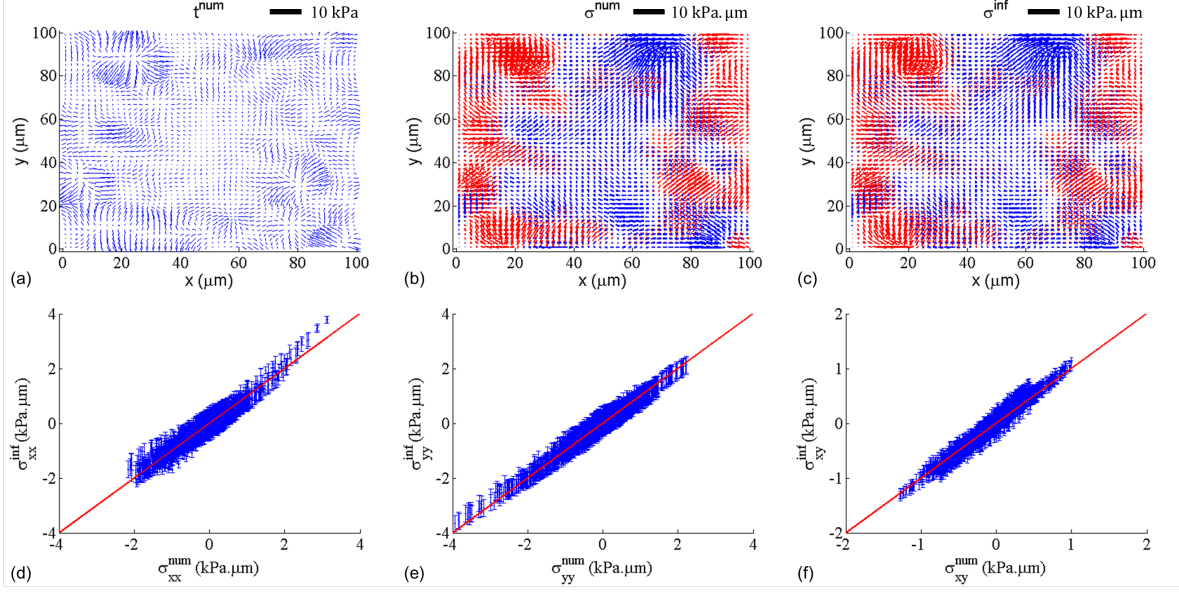


Figure 3: **Validation: numerical data.** (a) Simulated traction force field t^{num} , represented at each point by an arrow. Scale bar: 10 kPa. (b) Simulated stress field σ^{num} . (c) Inferred stress field σ^{inf} , plotted on a 50×50 grid. At each point, the stress tensor is represented by two line segments oriented along the stress eigenvectors, of lengths proportional to the eigenvalues (blue: tensile stress, red: compressive stress, scale bar: 10 kPa μm). Note the high degree of similarity between images (b) and (c). (d-f) Plots of the inferred stress *vs.* the simulated stress for each component, in kPa μm . Error bars correspond to $\delta\hat{\sigma}$ and the red line is the bisector $y = x$. To see this figure in color, go online.

All qualitative and quantitative indicators show that the stress field has been inferred accurately.

3.2 Robustness to variations of the statistical model

We test the robustness of BISM by varying *one by one* each feature of the statistical model, first focusing on alternative definitions of the prior, arguably our most prominent assumption, second modifying the likelihood, the hyperprior and the resolution method. For conciseness, precise definitions and implementations are given in *ST 2.1-2.3*. Table S1 in the Supporting Material lists the values of R_{σ}^2 thus obtained, given the same numerical data sets as for BISM.

Setting α_{xy} to 0 in the definition of the prior has a significant influence on the accuracy of inference ($R_{\sigma}^2 = 0.75$): the symmetry of the stress tensor needs to be enforced in the prior for accurate estimation. Unsurprisingly, this impacts less the diagonal ($R_{xx}^2 = R_{yy}^2 = 0.81$) than the shear components ($R_{xy}^2 = R_{yx}^2 = 0.61$). In a similar way, knowledge

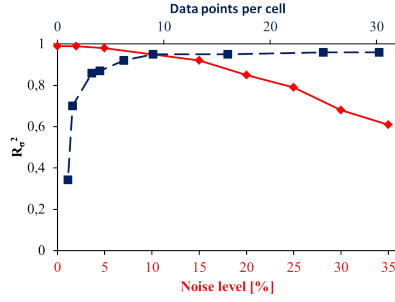


Figure 4: **Robustness.** BISM remains highly accurate ($R^2_\sigma > 0.8$) for noise levels and spatial resolutions typical of traction force measurements. Red solid line: coefficient of determination R^2_σ vs. relative level of added noise. R^2_σ is averaged over 3 realizations of the noise. Blue dashed line: coefficient of determination R^2_σ vs. number of traction force data points per cell, for a typical cell area of $100 \mu\text{m}^2$. To see this figure in color, go online.

of the correct boundary conditions should be included in the prior whenever possible: setting α_{BC} to 0 has a large negative impact ($R^2_\sigma = 0.53$). We shall further comment below on the influence of boundary conditions.

Importantly, the accuracy of inference remains excellent when the prior, the likelihood, or the hyperprior distributions are not Gaussian. This shows that the accuracy of BISM does not depend sensitively on a Gaussian assumption. Of note, we do not assume that traction force *data* obeys a Gaussian distribution. The data set ($\{t^{\text{num}}\}$ or $\{t^{\text{exp}}\}$) is used *as is* – indeed experimental traction force distributions are known to exhibit exponential tails [5, 63]. In all cases, the regularization parameter is small $\Lambda_{(\infty)} \ll 1$ (see Table S3 in the Supporting Material): the distribution of inferred stresses $\{\sigma^{\text{inf}}\}$ depends mostly on the empirical distribution of traction force data. Thus, even if the multivariate posterior distribution is Gaussian, the univariate, empirical distribution of the inferred stress (the mode $\bar{\sigma}_{\text{II}(\infty)}$) is not necessarily Gaussian (see Fig. S7 in the Supporting Material for numerical data). Similarly, even if the stress prior distribution function has a zero mean, the mean inferred stress is not necessarily equal to zero (see Fig. 5i for an example). The small values of $\Lambda_{(\infty)}$ are consistent with robustness with respect to variations of the prior.

We conclude that BISM is robust to variations of the statistical model.

3.3 Robustness to variations of the numerical simulation

We next apply BISM to a broad spectrum of numerical data, and vary successively the values of material parameters, the rheology, the boundary conditions, the system shape, the spatial resolution, the nature and the amplitude of the measurement noise (see *ST 2.2*).

Given the values of R^2_σ compiled in Table S2 in the Supporting Material, we verify that BISM remains accurate with a different (elastic) rheology (also set *Elastic 1* in Table 1),

or in a different (circular) geometry. In the viscous case, we observe that the accuracy decreases as a function of the bulk viscosity η' . For larger η' , we observe larger values of stress components, leading to asymmetrical distributions: this is at variance with our assumption of an even prior distribution, and may explain the lower value of R_σ^2 obtained when $\eta' = 10^1 \eta$.

Accuracy decreases when the prior does not include our knowledge of the boundary conditions. However the influence of erroneous values of the stress at the system's boundaries rapidly decreases far from the edge. When the coefficient α_{BC} is set to 0, removing the outtermost rows and columns increases R_σ^2 from 0.53 to 0.60. We estimate the corresponding “penetration length” of boundary values to about 10% of the system size, consistent with [34]. We conclude that, whenever available, the correct boundary conditions should be taken into account in the prior.

Importantly (see Fig. 4), accuracy remains acceptable ($R_\sigma^2 > 0.8$) for a spatial resolution larger than a few data points per cell, as well as for measurement noise levels up to 20 % of the traction force amplitude, consistent with measurement errors typical of force traction microscopy [31].

These results highlight that BISM is robust to variations of the numerical simulations that yield the traction force data.

3.4 Validation: experimental data

While inverting the force balance equations (1) requires specific techniques in 2D, the same problem reduces in 1D to straightforward integration along the spatial coordinate [5]. For this reason, we fabricated a micro-patterned ring whose measured mean radius $r_{\text{mean}} = 90 \mu\text{m}$ is larger than its width $w = 33 \mu\text{m}$, measured the substrate displacement field, and deduced the traction forces exerted by a monolayer of MDCK cells confined within the ring (Figs. 5a-c, see *Experimental Methods* for further details). We find an average traction force amplitude $t_{\text{exp}} \approx 200 \text{ Pa}$ for a measurement error of the order of $\delta t_{\text{exp}} \approx 40 \text{ Pa}$, and deduce a relative error $\delta t_{\text{exp}}/t_{\text{exp}}$ of the order of 20 %, consistent with the range of noise amplitudes where BISM was deemed applicable, see Fig. 4. The height of the monolayer is typically $5.3 \pm 1.2 \mu\text{m}$ (see Sec. 2.4), much smaller than the spatial extension $2\pi r_{\text{mean}}$, and varies smoothly, see Fig. S8 in the Supporting Material. In Figs. 5d-f, we plot the three stress components as inferred by BISM, with a regularization parameter $\Lambda_{(\infty)} = 6.7 \cdot 10^{-6}$ and a traction force-based measure of accuracy $\chi_T^2 = 4.7 \cdot 10^{-6}$, as defined by Eq. (22). Note that the inferred stresses are mostly positive, even though the prior distribution is a zero-mean Gaussian, see Fig. 5i.

Since shear stresses are small compared to angular normal stresses $|\sigma_{r\theta}|, |\sigma_{\theta r}| \ll |\sigma_{\theta\theta}|$, the orthoradial component of the force balance equation (see *ST 1.2*) simplifies to

$$\frac{\partial \sigma_{\theta\theta}}{\partial \theta} = r t_\theta \quad (23)$$

Taking into account the experimental angular resolution $\Delta\theta$, and averaging radially over the width of the ring, we obtain the 1D value of the increment of orthoradial stress over $\Delta\theta$:

$$\Delta\sigma_{\theta\theta}^{\text{1D}} = \langle r t_\theta \rangle_r \Delta\theta \quad (24)$$

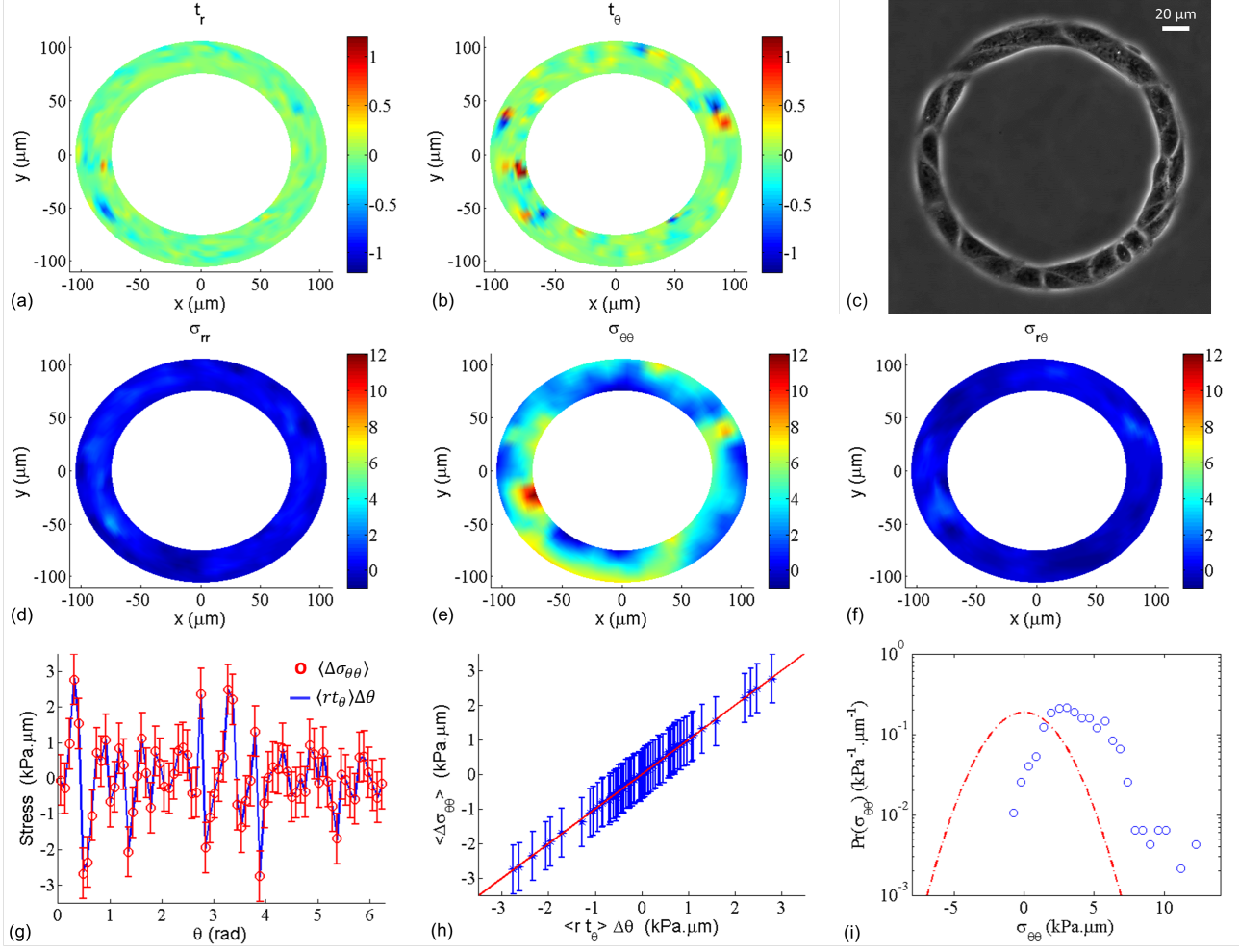


Figure 5: **Validation: experimental data.** (a-b) Heat maps of the components t_r and t_θ of the traction forces t^{exp} in kPa, on a 12×72 polar grid. (c) Phase contrast image of the MDCK cell monolayer. Scale bar: 20 μm . (d-f) Heat maps of the components σ_{rr} , $\sigma_{\theta\theta}$ and $\sigma_{r\theta}$ of the inferred stress field σ^{inf} in $\text{kPa}\cdot\mu\text{m}$. (g) Angular profiles of the radially-averaged inferred stress ($\langle \Delta\sigma_{\theta\theta} \rangle_r$, red circles) and of the 1D stress ($\langle r t_\theta \rangle_r \Delta\theta$, blue line), with an angular resolution $\Delta\theta = \pi/36$ rad. Error bars of the inferred stress are the radial average of $\delta\hat{\sigma}_{\theta\theta}$. (h) Radially-averaged inferred stress *vs.* the 1D stress. The coefficient of determination of this plot is $R_{\text{ring}}^2 = 0.99$. (i) Empirical distribution function of the inferred component $\sigma_{\theta\theta}$ (blue circles). The red dashed line corresponds to the zero-mean, Gaussian prior distribution function with standard deviation $s_0 = 2.13 \text{ kPa}\cdot\mu\text{m}$. To see this figure in color, go online.

This value is compared with the radially-averaged increment of orthoradial stress inferred by BISM $\langle \Delta\sigma_{\theta\theta} \rangle_r$ (Figs. 5g-h). The excellent agreement found between experimental ($\langle r t_\theta \rangle_r \Delta\theta$) and inferred ($\langle \Delta\sigma_{\theta\theta} \rangle_r$) 1D stresses is quantified by a coefficient of determina-

tion $R_{\text{ring}}^2 = 0.99$, see Fig. 5h. To check that BISM allows to infer absolute stress values, we calculate the average pressure $\langle P_{\text{exp}} \rangle$ from traction force data (see *ST 1.4*):

$$\langle P_{\text{exp}} \rangle = \frac{1}{2} \langle t_r r \rangle \quad (25)$$

where $\langle \rangle$ denotes spatial averaging over the whole domain. We obtain $\langle P_{\text{exp}} \rangle = -2.18 \text{ kPa} \cdot \mu\text{m}$, in agreement with the average inferred pressure $\langle P_{\text{inf}} \rangle = -2.17 \pm 0.94 \text{ kPa} \cdot \mu\text{m}$.

We conclude that BISM is readily applicable to experimental traction force data, and has been validated on experimental data without reference to a specific rheological model of the tissue.

3.5 Comparison with monolayer stress microscopy

Monolayer stress microscopy, as introduced in [26], assumes that the cell monolayer is a linear, isotropic elastic body. Given traction force data, MSM consists in finding the stress field that minimizes an energy functional of the cell monolayer. MSM is thus straightforward to implement using **FreeFem++** [64], a finite element software based on the same variational approach (see *ST 1.1*).

A simpler implementation of MSM, that also assumes an elastic cell monolayer rheology, has been proposed recently [36]. We call this method **MSMu** since it does not require the calculation of traction forces and uses the substrate displacement field u as input data. **MSMu** further assumes that the displacement field u is continuous at the interface between substrate and cells: tissue internal stresses are computed directly from substrate displacements. In practice, we calculate substrate displacements from the traction force data set, given numerical values of the substrate elastic modulus $E_{\text{sub}} = 5 \text{ kPa}$ and Poisson ratio $\nu_{2\text{D sub}} = 0.5$ [36].

By analogy with MSM, we introduce a stress estimation method, named **MSM η** , that assumes a viscous rheology for the cell monolayer. Thanks to the variational formulation, we compute the velocity field given the force traction field with **FreeFem++**, and estimate the stress field given numerical values of the viscosity coefficients. Of note, other variants of MSM could be implemented assuming other tissue rheologies consistent with a variational formulation [65].

The comparison relies on three numerical simulations: in addition to the *Viscous* and *Elastic 1* data sets studied above, another simulation of an elastic tissue, named *Elastic 2*, has been performed, using the elastic coefficients $E = 10 \text{ kPa} \cdot \mu\text{m}$ and $\nu_{2\text{D}} = 0.5$, as advocated in [36]. Each variant of MSM assumes a tissue rheology, and thus relies on a set of material parameters. To perform MSM and **MSMu**, we use the same tissue elastic coefficients as in the *Elastic 1* [26] and *Elastic 2* [36] simulations respectively. To perform **MSM η** , we use the same tissue viscosity coefficients as in the *Viscous* simulation.

Table 1 summarizes our results and compares the accuracy of the different methods (see also Fig. S9 in the Supporting Material for visual comparison). In all cases, the values of R_{σ}^2 are closer to 1 for BISM, which performs better than MSM, **MSMu** and **MSM η** . By construction, BISM seems less sensitive to experimental noise than deterministic stress microscopies. For each variant of MSM, accuracy is maximal for the data set generated

Rheology	BISM	MSM	MSMu	MSM η
<i>Viscous</i>	0.96	-0.52	0.48	0.91
<i>Elastic 1</i>	0.97	0.88	0.73	0.80
<i>Elastic 2</i>	0.99	0.61	0.85	0.67

Table 1: **Comparison with monolayer stress microscopy.** Coefficients of determination R_σ^2 obtained with BISM, MSM, MSMu and MSM η (see text for definitions). Traction force data sets were obtained with material parameter values $\eta = 10^3 \text{ kPa } \mu\text{m s}$, $\eta' = \eta$ (*Viscous*); $E = 10^2 \text{ kPa } \mu\text{m}$, $\nu_{2D} = 0.5$ [26] (*Elastic 1*), $E = 10 \text{ kPa } \mu\text{m}$, $\nu_{2D} = 0.5$ [36] (*Elastic 2*). A white noise of relative amplitude 5% is added in all cases.

according to the same rheological hypothesis, *i.e.* *Elastic 1*, *Elastic 2* and *Viscous* for MSM, MSMu and MSM η respectively. Unsurprisingly, a mismatch between numerical simulation and stress microscopy methods, either in the values of material parameters or in the choice of a rheology, leads to a lower value of the coefficient of determination.

We also applied MSM to the experimental data set studied in *Validation: experimental data*. Following the same protocol, we obtained a larger dispersion of inferred values than with BISM. The inferred data set obtained by MSM is characterized by a lower coefficient of determination $R_{\text{ring}}^2 = 0.32$, far below the BISM value $R_{\text{ring}}^2 = 0.99$.

All existing stress microscopies infer the stress field up to an additive null vector σ^0 such that $\text{div } \sigma^0 = 0$. Classically [53], null vectors of the linear problem $\text{div } \sigma = \vec{t}$ are related to the Airy stress function χ through $\sigma_{xx}^0 = \frac{\partial^2 \chi}{\partial y^2}$, $\sigma_{yy}^0 = \frac{\partial^2 \chi}{\partial x^2}$ and $\sigma_{xy}^0 = -\frac{\partial^2 \chi}{\partial x \partial y}$. Since BISM infers faithfully the mean stress $\langle \sigma \rangle$ in confined geometries, it limits the class of undetectable stresses to *zero-mean* stress fields that verify both $\text{div } \sigma^0 = 0$ and the boundary conditions (4). Alternative methods will be necessary to ascertain the relevance of these special solutions to cell monolayer mechanics.

4 Conclusion

Bayesian inversion stress microscopy estimates the internal stress field of a cell monolayer given traction force data. Validation on both numerical and experimental data shows that the method works reliably independently of the tissue rheology, of its geometry, and of the boundary conditions imposed on the stress field. As a consequence, BISM should apply equally well to isolated cell assemblies and to patches of cells within a larger monolayer. Since the hypotheses made pertain to statistics (Bayesian inversion), we checked that the method is robust to changes in the underlying statistical model, in particular to changes in the prior. Importantly, its statistical nature leads to a simple, natural definition of an error bar on the stress estimate. It is compatible with the level of experimental noise and with the spatial resolution typical of traction force microscopy. Last, BISM is more accurate than MSM, and its accuracy is less sensitive to the rheology of the tissue than all variants of monolayer stress microscopy. BISM is quite general since

it relies on the laws of mechanics and on reasonable and robust statistical assumptions. It can therefore be applied to other active materials strongly interacting with a soft substrate, provided that the height of the system is small compared to its planar spatial extension.

We analyzed traction force *images*, *i.e.* spatial data at a given, fixed time. However, BISM does not rely on an assumption of quasi-stationarity, and would apply equally well to spatio-temporal data, *i.e.* to traction force *movies*. Our preliminary results suggest that combining Bayesian inversion with Kalman filtering then further improves accuracy.

To date, the modeling of cell monolayer mechanics typically relies on a *forward* approach: assumptions made on tissue rheology are validated indirectly through predictions made on (measurable) tissue kinematics. A reliable measurement of the internal stress field paves the way to *inverse* approaches, where the combination of stress with kinematic data, such as the strain rate field or the cell-neighbour exchange rate field, would allow to read out constitutive equations from data, and to infer the values of material parameters.

Acknowledgements

We would like to thank Cyprien Gay, François Graner, Yohei Kondo and Sham Tlili for stimulating discussions.

Financial supports from the Human Frontier Science Program (grant RGP0040/2012), the European Research Council under the European Union's Seventh Framework Programme (FP7/2007-2013)/ERC grant agreement n° 617233, and the Mechanobiology Institute are gratefully acknowledged. S.J. acknowledges the Merlion-2014 programme of the French Ministry of Foreign Affairs. B.L. acknowledges the Institut Universitaire de France.

References

- [1] Ray Keller, Lance Davidson, ..., and Paul Skoglund. Mechanisms of convergence and extension by cell intercalation. *Phil Trans R Soc Lond B*, 897-922:355, 2000.
- [2] Laurens G. van der Flier and Hans Clevers. Stem cells, self-renewal, and differentiation in the intestinal epithelium. *Annu Rev Physiol*, 75:241–260, 2009.
- [3] Peter Friedl and Darren Gilmour. Collective cell migration in morphogenesis, regeneration and cancer. *Nat. Rev. Cell Mol. Biol.*, 10:445–457, 2009.
- [4] M. Poujade, E. Grasland-Mongrain, ..., P. Silberzan. Collective migration of an epithelial monolayer in response to a model wound. *Proc Natl Acad Sci USA*, 104:15988–15993, 2007.
- [5] Xavier Trepate, Michael R. Wasserman, ..., Jeffrey J. Fredberg. Physical forces during collective cell migration. *Nat Phys*, pages 426 – 430, 2009.

- [6] Ester Anon, Xavier Serra-Picamal, ..., Benoit Ladoux. Cell crawling mediates collective cell migration to close undamaged epithelial gaps. *Proc Natl Acad Sci USA*, 109:10891–10896, 2012.
- [7] Olivier Cochet-Escartin, Jonas Ranft, ..., Philippe Marcq. Border forces and friction control epithelial closure dynamics. *Biophys J*, 106:65–73, 2014.
- [8] Sri Ram Krishna Vedula, Man Chun Leong, ..., Benoit Ladoux. Emerging modes of collective cell migration induced by geometrical constraints. *Proc Natl Acad Sci U S A*, 109:12974–12979, 2012.
- [9] Anna-Kristina Marel, Matthias Zorn, ..., Joachim O Rädler. Flow and diffusion in channel-guided cell migration. *Biophys J*, 107:1054–1064, 2014.
- [10] Kevin Doxzen, Sri Ram Krishna Vedula, ..., Chwee Teck Lim. Guidance of collective cell migration by substrate geometry. *Integr Biol*, 5:1026–1035, 2013.
- [11] M. Deforet, V. Hakim, ..., P. Silberzan. Emergence of collective modes and tri-dimensional structures from epithelial confinement. *Nat Commun*, 5:3747, 2014.
- [12] William J Ashby and Andries Zijlstra. Established and novel methods of interrogating two-dimensional cell migration. *Integr Biol*, 4:1338–1350, 2012.
- [13] Sri Ram Krishna Vedula, Andrea Ravasio, ..., Benoit Ladoux. Collective cell migration: a mechanistic perspective. *Physiology*, 28:370–379, 2013.
- [14] Benoit Ladoux and Alice Nicolas. Physically based principles of cell adhesion mechanosensitivity in tissues. *Rep Prog Phys*, 75:116601, 2012.
- [15] Zhijun Liu, John L Tan, ..., Christopher S Chen. Mechanical tugging force regulates the size of cell-cell junctions. *Proc Natl Acad Sci USA*, 107:9944–9949, 2010.
- [16] Elsa Bazellières, Vito Conte, ..., Xavier Trepast. Control of cell-cell forces and collective cell dynamics by the intercellular adhesome. *Nat Cell Biol*, 17:409–420, 2015.
- [17] K. Sugimura, F. Graner, and P.-F. Lenne. Measuring forces and stresses in situ in living tissues. *bioRxiv*, 016394, 2015.
- [18] Carsten Grashoff, Brenton D Hoffman, ..., Martin A Schwartz. Measuring mechanical tension across vinculin reveals regulation of focal adhesion dynamics. *Nature*, 466:263–266, 2010.
- [19] Nicolas Borghi, Maria Sorokina, ..., Alexander R Dunn. E-cadherin is under constitutive actomyosin-generated tension that is increased at cell–cell contacts upon externally applied stretch. *Proc Natl Acad Sci USA*, 109:12568–12573, 2012.
- [20] Thomas P Kole, Yiider Tseng, and Denis Wirtz. Intracellular microrheology as a tool for the measurement of the local mechanical properties of live cells. *Methods Cell Biol*, 78:45–64, 2004.

- [21] Monica Tanase, Nicolas Biais, and Michael Sheetz. Magnetic tweezers in cell biology. *Meth Cell Biol*, 83:473–493, 2007.
- [22] Otger Campàs, Tadanori Mammoto, ..., Donald E Ingber. Quantifying cell-generated mechanical forces within living embryonic tissues. *Nat Meth*, 11:183–189, 2014.
- [23] Ulrike Nienhaus, Tinri Aegerter-Wilmsen, and Christof M Aegerter. Determination of mechanical stress distribution in drosophila wing discs using photoelasticity. *Mech Dev*, 126:942–949, 2009.
- [24] Matteo Rauzi, Pascale Verant, ..., Pierre-François Lenne. Nature and anisotropy of cortical forces orienting drosophila tissue morphogenesis. *Nat Cell Biol*, 10:1401–1410, 2008.
- [25] Isabelle Bonnet, Philippe Marcq, ..., François Graner. Mechanical state, material properties and continuous description of an epithelial tissue. *J Roy Soc Interface*, 9:2614–2623, 2012.
- [26] Dhananjay T Tambe, C. Corey Hardin, ..., Xavier Trepate. Collective cell guidance by cooperative intercellular forces. *Nat Mater*, 10:469–475, 2011.
- [27] Davide Ambrosi, Alain Duperray, Valentina Peschetola, and Claude Verdier. Traction patterns of tumor cells. *J Math Biol*, 58:163–181, 2009.
- [28] Robert W Style, Rostislav Boltyskiy, ..., Eric R Dufresne. Traction force microscopy in physics and biology. *Soft Matter*, 10:4047–4055, 2014.
- [29] Micah Dembo and Yu-Li Wang. Stresses at the cell-to-substrate interface during locomotion of fibroblasts. *Biophys J*, 76:2307–2316, 1999.
- [30] James P Butler, Iva Marija Tolić-Norrelykke, ..., Jeffrey J Fredberg. Traction fields, moments, and strain energy that cells exert on their surroundings. *Am J Physiol Cell Physiol*, 282:C595–C605, 2002.
- [31] Nathan J Sniadecki and Christopher S Chen. Microfabricated silicone elastomeric post arrays for measuring traction forces of adherent cells. *Methods Cell Biol*, 83:313–328, 2007.
- [32] Olivia Du Roure, Alexandre Saez, ..., Benoit Ladoux. Force mapping in epithelial cell migration. *Proc Natl Acad Sci USA*, 102:2390–2395, 2005.
- [33] A Saez, E Anon, ..., B Ladoux. Traction forces exerted by epithelial cell sheets. *J Phys: Cond Matt*, 22:194119, 2010.
- [34] Dhananjay T Tambe, Ugo Croutelle, ..., Jeffrey J Fredberg. Monolayer stress microscopy: limitations, artifacts, and accuracy of recovered intercellular stresses. *PLoS One*, 8:e55172, 2013.

- [35] Juliane Zimmermann, Ryan L Hayes, ..., Herbert Levine. Intercellular stress reconstitution from traction force data. *Biophys J*, 107:548–554, 2014.
- [36] Michel Moussus, Christelle der Loughian, ..., Alice Nicolas. Intracellular stresses in patterned cell assemblies. *Soft Matt*, 10:2414–2423, 2014.
- [37] Jonas Ranft, Markus Basan, ..., Frank Jülicher. Fluidization of tissues by cell division and apoptosis. *Proc Natl Acad Sci U S A*, 107:20863–20868, 2010.
- [38] Julia C Arciero, Qi Mi, ..., David Swigon. Continuum model of collective cell migration in wound healing and colony expansion. *Biophys J*, 100:535–543, 2011.
- [39] Pilhwa Lee and Charles W Wolgemuth. Crawling cells can close wounds without purse strings or signaling. *PLoS Comput Biol*, 7:e1002007, 2011.
- [40] Michael H. Köpf and Len M. Pismen. A continuum model of epithelial spreading. *Soft Matter*, 9:3727–3734, 2012.
- [41] Sri Ram Krishna Vedula, Hiroaki Hirata, ..., Benoit Ladoux. Epithelial bridges maintain tissue integrity during collective cell migration. *Nat Mat*, 13:87–96, 2014.
- [42] Jari Kaipio and Erkki Somersalo. *Statistical and computational inverse problems*. Springer, 2006.
- [43] A. M. Stuart. Inverse problems: A bayesian perspective. *Acta Numer*, 19:451–559, 2010.
- [44] Udo von Toussaint. Bayesian inference in physics. *Rev Mod Phys*, 83:943–999, 2011.
- [45] Akatsuki Kimura, Antonio Celani, ..., Kazuyuki Nakamura. Estimating cellular parameters through optimization procedures: elementary principles and applications. *Front Physiol*, 6, 2015.
- [46] Micah Dembo, Tim Oliver, ..., K Jacobson. Imaging the traction stresses exerted by locomoting cells with the elastic substratum method. *Biophys J*, 70:2008, 1996.
- [47] Jérôme RD Soiné, Christoph A Brand, ..., Deshpande Vikram. Model-based traction force microscopy reveals differential tension in cellular actin bundles. *PLoS Comput Biol*, 11:e1004076, 2015.
- [48] Shuji Ishihara and Kaoru Sugimura. Bayesian inference of force dynamics during morphogenesis. *J Theor Biol*, 313:201–211, 2012.
- [49] Kaoru Sugimura and Shuji Ishihara. The mechanical anisotropy in a tissue promotes ordering in hexagonal cell packing. *Dev*, 140:4091–4101, 2013.
- [50] S. Ishihara, K. Sugimura, ..., F. Graner. Comparative study of non-invasive force and stress inference methods in tissue. *Eur Phys J E*, 36:9859, 2013.

- [51] Kevin K Chiou, Lars Hufnagel, and Boris I Shraiman. Mechanical stress inference for two dimensional cell arrays. *PLoS Comput Biol*, 8:e1002512, 2012.
- [52] G. Wayne Brodland, Jim H Veldhuis, ..., M. Shane Hutson. Cellfit: A cellular force-inference toolkit using curvilinear cell boundaries. *PLoS One*, 9:e99116, 2014.
- [53] LD Landau and EM Lifshitz. *Elasticity theory*. Pergamon Press, 1975.
- [54] S. M. Zehnder, M. Suaris, M. M. Bellaire and T. E. Angelini (2015). Cell volume fluctuations in MDCK monolayers. *Biophys J*, 108(2), 247-250, 2015.
- [55] U. S. Schwarz, N. Q. Balaban, ..., S. A. Safran. Calculation of forces at focal adhesions from elastic substrate data: the effect of localized force and the need for regularization. *Biophys J*, 83:1380–1394, 2002.
- [56] Bradley P Carlin and Thomas A Louis. *Bayesian methods for data analysis*. Chapman & Hall, 2008.
- [57] Andrew Gelman, John B Carlin, Donald B Rubin. *Bayesian data analysis*. Taylor & Francis, 2014.
- [58] Sri Ram Krishna Vedula, Andrea Ravasio, ..., Benoit Ladoux. Microfabricated environments to study collective cell behaviors. *Methods Cell Biol*, 120:235–252, 2014.
- [59] Jenny Fink, Manuel Théry, ..., Matthieu Piel. Comparative study and improvement of current cell micro-patterning techniques. *Lab Chip*, 7:672–680, 2007.
- [60] K Li. The image stabilizer for ImageJ. 2008.
- [61] Jean-Louis Martiel, Aldo Leal, ..., Manuel Théry. Measurement of cell traction forces with ImageJ. *Methods Cell Biol*, 125:269–287, 2015.
- [62] Andrew R Harris, Loic Peter, ..., Guillaume T Charras. Characterizing the mechanics of cultured cell monolayers. *Proc Natl Acad Sci U S A*, 109:16449–16454, 2012.
- [63] N. S. Gov. Traction forces during collective cell motion. *HFSP Journal*, 3:223–227, 2009.
- [64] Frédéric Hecht. New development in FreeFem++. *J Num Math*, 20:251–266, 2012.
- [65] Sham Tlili, Cyprien Gay, ..., Pierre Saramito. Mechanical formalisms for tissue dynamics. *Eur Phys J E*, 38:121, 2015.
- [66] LD Landau and EM Lifshitz. *Fluid mechanics*. Pergamon Press, 1987.
- [67] AD Jenkins and KB Dysthe. The effective film viscosity coefficients of a thin floating fluid layer. *J Fluid Mech*, 109:108101, 1997.

- [68] Albert Tarantola. *Inverse problem theory and methods for model parameter estimation*. SIAM, 2005.
- [69] G.J. McLachlan and T. Krishnan. *The EM algorithm and its extensions*. Wiley, 2008.
- [70] Morgan Delarue, Jean-François Joanny, ..., Jacques Prost. Stress distributions and cell flows in a growing cell aggregate. *Interface Focus*, 4:33, 2014.
- [71] Shiladitya Banerjee and M Cristina Marchetti. Contractile stresses in cohesive cell layers on finite-thickness substrates. *Phys Rev Lett*, 109:108101, 2012.
- [72] Torbjørn Eltoft, Taesu Kim, and Te-Won Lee. On the multivariate laplace distribution. *Signal Proc Lett IEEE*, 13:300–303, 2006.
- [73] Matthew James Beal. *Variational algorithms for approximate Bayesian inference*. University of London, 2003.
- [74] Michael E Tipping. Sparse bayesian learning and the relevance vector machine. *J Mach Learn Res*, 1:211–244, 2001.
- [75] Per Christian Hansen. Analysis of discrete ill-posed problems by means of the L-curve. *SIAM Review*, 34:561–580, 1992.

SUPPORTING TEXT

1 Computational aspects

1.1 Numerical simulations

We use the finite element software **FreeFem++** [64] to solve numerically the conservation equations and generate stress and traction force data for several rheologies (viscous and elastic) and several geometries (square and disc). **FreeFem++** requires the weak formulation of evolution equations. The momentum conservation equation $\text{div } \sigma = \vec{t}$ reads in variational form

$$\int_{\Omega} \vec{\nabla} \sigma \cdot \vec{w} = \int_{\Omega} \vec{t} \cdot \vec{w}$$

where \vec{w} is a vector test function and Ω is the domain of integration. The boundary conditions $\sigma \cdot \vec{n} = \vec{0}$, where \vec{n} denotes the vector normal to the edge, are implemented through an extra term integrated over the boundary $\delta\Omega$

$$\int_{\Omega} \vec{\nabla} \sigma \cdot \vec{w} = \int_{\Omega} \vec{t} \cdot \vec{w} + \int_{\delta\Omega} \sigma \vec{n} \cdot \vec{w}$$

Viscous liquid

The constitutive equation of a viscous, compressible liquid reads [66]

$$\sigma = \eta \left(\vec{\nabla} \vec{v} + (\vec{\nabla} \vec{v})^t \right) + \eta' \left(\vec{\nabla} \cdot \vec{v} \right) I$$

where η and η' are the shear and compression coefficients of viscosity. Taking into account friction with the substrate, with a friction coefficient ξ_v , and a motility force field \vec{f}_{act} , the total traction force \vec{t} reads

$$\vec{t} = \xi_v \vec{v} - \vec{f}_{\text{act}}$$

The active force \vec{f}_{act} is generated by n_d force dipoles randomly distributed in space, see below.

Using the momentum conservation equation, we obtain an equation on \vec{v}

$$-\eta \Delta \vec{v} - (\eta + \eta') \vec{\nabla} (\vec{\nabla} \cdot \vec{v}) + \xi_v \vec{v} = \vec{f}_{\text{act}}$$

whose weak form reads

$$\int_{\Omega} \eta \vec{\nabla} \vec{v} \cdot \vec{\nabla} \vec{w} - \int_{\Omega} (\eta + \eta') \vec{\nabla} (\vec{\nabla} \cdot \vec{v}) \cdot \vec{w} + \int_{\Omega} \xi_v \vec{v} \cdot \vec{w} = \int_{\Omega} \vec{f}_{\text{act}} \cdot \vec{w}$$

We solve this equation for the velocity field with **FreeFem++** on a $100 \times 100 \mu\text{m}^2$ square with boundary conditions $\sigma \cdot \vec{n} = \vec{0}$, and with material parameter values typical of cell monolayers: $\xi_v = 10^0 \text{ kPa } \mu\text{m}^{-1}\text{s}$ [7], $\eta = 10^3 \text{ kPa } \mu\text{m s}$ [62], $\eta' = \eta$. To the best of our knowledge, the second coefficient of viscosity η' has not been measured in a tissue, but theoretical reasoning suggests $\eta' = 2\eta$ for a thin monolayer, due to 3D incompressibility [67]. The stress and traction force fields are derived from the velocity field and sampled over a regular cartesian grid with $C = R = 50$ and $N = C \times R = 2500$ (see Fig. 3a-b).

Elastic solid

In the limit of small deformations, the constitutive equation of an elastic body reads [53]

$$\sigma = \mu \left(\vec{\nabla} \vec{u} + (\vec{\nabla} \vec{u})^t \right) + \lambda (\vec{\nabla} \cdot \vec{u}) I$$

with Lamé coefficients λ, μ . With a (solid) friction force proportional to the displacement, the traction force reads $\vec{t} = \xi_u \vec{u} - \vec{f}_{act}$, and the momentum conservation equation

$$-\mu \Delta \vec{u} - (\mu + \lambda) \vec{\nabla} (\vec{\nabla} \cdot \vec{u}) + \xi_u \vec{u} = \vec{f}_{act}$$

is formally identical to that obtained for the flow of a viscous liquid, substituting \vec{v} by \vec{u} and the material parameters η, η', ξ_v by μ, λ, ξ_u . The numerical resolution is therefore similar to that described above for a viscous liquid. Parameter values differ: for instance a realistic Poisson ratio $\nu_{2D} = \frac{\lambda}{\lambda + 2\mu} = 0.5$ imposes $\lambda = 2\mu$.

Active forces

The active force \vec{f}_{act} is generated by n_d force dipoles defined in tensor form as

$$p^n(\vec{x}) = \left[p_{tr}^n \begin{pmatrix} 1 & 0 \\ 0 & 1 \end{pmatrix} - p_{dev}^n \begin{pmatrix} \cos 2\theta_n & \sin 2\theta_n \\ \sin 2\theta_n & -\cos 2\theta_n \end{pmatrix} \right] \delta(\vec{x} - \vec{x}_n), \quad n = 1, \dots, n_d$$

with positions \vec{x}_n , amplitudes p_{tr}^n and p_{dev}^n for the trace and deviator, and orientations θ_n . The dipole positions \vec{x}_n and orientations θ_n are random variables uniformly distributed over the spatial domain Ω and $[0, 2\pi]$ respectively. In practice, the force dipoles are implemented using a finite-size Gaussian approximation of the delta function, with a spatial extension $2d = 10 \mu\text{m}$ of the order of a typical cell size. The components of the active force read

$$f_{act,i}(\vec{x}) = \sum_{n=1}^{n_d} \partial_j p_{ij}^n(\vec{x})$$

with $n_d = 100$ force dipoles of typical amplitude 10^{-2} kPa [32]. Since the amplitude of traction forces is known to be larger close to the edge than in the bulk, the coefficients p_{tr}^n and p_{dev}^n are set proportional to $1 + r/l_p$, where r is the distance to the center of the domain and $l_p = 5 \mu\text{m}$ is a penetration length [32].

MSM implementation

Monolayer stress microscopy [26] consists in finding, given traction force data, the displacement field \vec{u} that verifies the force balance equation obtained for a purely elastic stress. Thanks to the hypothesis made on tissue rheology, the problem becomes well-posed since two components of the displacement vector are deduced from two components of the traction force vector. Once \vec{u} is known, the calculation of the stress depends on the numerical values of tissue elastic coefficients. We implement MSM with **FreeFem++**, solving the weak form

$$\int_{\Omega} \mu \vec{\nabla} \vec{u} \cdot \vec{\nabla} \vec{w} - \int_{\Omega} (\mu + \lambda) \vec{\nabla} (\vec{\nabla} \cdot \vec{u}) \cdot \vec{w} + \int_{\Omega} \vec{t} \cdot \vec{w} + \int_{\partial\Omega} (\sigma \vec{n}) \cdot \vec{w} = 0$$

for appropriate test functions \vec{w} , with numerical or experimental data sets of traction forces.

The variant MSM η assumes that the tissue has the rheology of a viscous liquid. It is well-posed for the same reason, and consists in solving the weak form of the “viscous” force balance equation

$$\int_{\Omega} \eta \vec{\nabla} \vec{v} \cdot \vec{\nabla} \vec{w} - \int_{\Omega} (\eta + \eta') \vec{\nabla} (\vec{\nabla} \cdot \vec{v}) \cdot \vec{w} + \int_{\Omega} \vec{t} \cdot \vec{w} + \int_{\partial\Omega} (\sigma \vec{n}) \cdot \vec{w} = 0$$

for the velocity field \vec{v} , from which the stress is computed given numerical values of the viscosities η and η' .

1.2 Polar coordinates

For cell monolayers confined within a ring, or within a disk, we use the polar coordinate system (r, θ) . The force balance equations for the stress tensor field $\sigma = \begin{pmatrix} \sigma_{rr} & \sigma_{r\theta} \\ \sigma_{r\theta} & \sigma_{\theta\theta} \end{pmatrix}$ and the traction force field $\vec{T} = \begin{pmatrix} t_r \\ t_\theta \end{pmatrix}$ read

$$\begin{aligned} \frac{1}{r} \frac{\partial(r\sigma_{rr})}{\partial r} + \frac{1}{r} \frac{\partial\sigma_{r\theta}}{\partial\theta} - \frac{\sigma_{\theta\theta}}{r} &= t_r \\ \frac{1}{r} \frac{\partial\sigma_{\theta\theta}}{\partial\theta} + \frac{1}{r} \frac{\partial(r\sigma_{\theta r})}{\partial r} + \frac{\sigma_{r\theta}}{r} &= t_\theta \end{aligned}$$

where, as for the cartesian coordinate system, we do not enforce the symmetry of the stress tensor.

When discretizing the derivatives with respect to r and θ to lowest order, the (cartesian) expression (8) for the matrix A is no longer valid and must be replaced by

$$A_{(r,\theta)} = \begin{pmatrix} A_r/r & -I/r & A_\theta/r & 0 \\ 0 & A_\theta/r & I/r & A_r/r \end{pmatrix}$$

where A_r and A_θ are sub-matrices that correspond to the discretized forms of the partial derivatives $\frac{\partial}{\partial r} r$ and $\frac{\partial}{\partial \theta}$ respectively.

1.3 Grids

Numerical data

In order to implement the mechanics of a rectangular piece of tissue on a grid G_i with C columns for the x coordinate and R rows for the y coordinate of traction force data, in reality we need to simulate a grid G_s with $2R + 1$ rows and $2C + 1$ columns, with two traction force components and four stress components at each point (see Fig. 1b). We extract from the odd-numbered columns and even-numbered rows the σ_{xx} and σ_{yx} components $((C + 1) \times R$ values), from the even-numbered columns and odd-numbered rows the σ_{yy} and σ_{xy} components $(C \times (R + 1)$ values) and finally from the even-numbered columns and even-numbered rows the t_x and t_y values $(C \times R$ values). When plotting the stress field, each stress component is interpolated (second order interpolation in l) at a position at the center of each grid cell to obtain the required $C \times R$ values. We use the same method in polar coordinates, replacing x by θ and y by r .

Experimental data

Irrespective of the method, each experimental traction force data point is associated with a given cell of the measurement grid G_m . We need to interpolate these experimental values on a regular grid G_i , either cartesian or polar depending on the geometry. For each cell of the numerical grid G_i , we first calculate the areas of intersection with cells of the initial grid G_m , and compute an average, weighted by these areas, over the traction forces in the cells of G_m with a non-zero overlap. This procedure yields the traction force in the cell of G_i , which we use for stress inference.

1.4 Average stress from traction force data

Spatially averaged values of stress components can be calculated directly from traction force data assuming the boundary condition $\sigma_{ij} n_j = 0$. For completeness sake, we adapt here the classical derivation [53] to the calculation of the average pressure in polar coordinates.

We use cartesian coordinates $(x_1, x_2) = (x, y)$, and summation over repeated indices is assumed throughout. Multiplying both terms of the force balance equation

$$\frac{\partial \sigma_{ij}}{\partial x_j} = t_i \quad (1)$$

by x_k , and integrating over the domain Ω , we obtain

$$\begin{aligned} \int_{\Omega} t_i x_k &= \int_{\Omega} \frac{\partial \sigma_{ij}}{\partial x_j} x_k \\ &= \int_{\Omega} \frac{\partial}{\partial x_j} (\sigma_{ij} x_k) - \int_{\Omega} \sigma_{ij} \frac{\partial x_k}{\partial x_j} \\ &= \int_{\partial\Omega} \sigma_{ij} x_k n_j - \int_{\Omega} \sigma_{ik} \\ &= 0 - \int_{\Omega} \sigma_{ik} \end{aligned}$$

where we used $\frac{\partial x_k}{\partial x_j} = \delta_{kj}$ and $\sigma_{ij} n_j = 0$. Denoting as usual spatial averages by brackets $\langle \dots \rangle$, we find [53]:

$$\langle \sigma_{ik} \rangle = -\langle t_i x_k \rangle. \quad (2)$$

In the case of the numerical simulation leading to Fig. 3, we checked that the average inferred stress values $\langle \sigma_{ik}^{\text{inf}} \rangle$ agree with the values $\langle \sigma_{ik}^{\text{num}} \rangle$ computed directly from the numerical traction force data using (2).

We next calculate the average pressure, invariant under a change of coordinate system since $P = -\frac{1}{2} \text{Tr} \sigma$:

$$\begin{aligned} \langle P \rangle &= -\frac{1}{2} (\langle \sigma_{xx} \rangle + \langle \sigma_{yy} \rangle) \\ &= \frac{1}{2} (\langle t_x x \rangle + \langle t_y y \rangle) \end{aligned}$$

Switching to polar coordinates, we obtain

$$\langle P \rangle = \frac{1}{2} \langle t_{rr} \rangle. \quad (3)$$

2 Robustness

We describe here the variations performed on BISM in order to test its robustness, by varying *one by one* each feature of the statistical model (Secs. 2.1), and of the numerical simulation (Sec. 2.2). Precise definitions and implementations of the statistical models are given in Sec. 2.3.

2.1 Robustness to variations of the statistical model

Variations made on the prior are the following.

(i) Distribution of the stress

P1 Laplace prior: amounts to regularization with a L_1 norm [68].

P2 Smoothness prior: penalizes spatial variations of the stress field [42].

P3 Unequal standard deviations $s_0^{\text{tr}} \neq s_0^{\text{dev}}$ for the trace and deviator of the stress.

P4 Non-zero mean value of the stress: $\sigma_0 = \begin{pmatrix} \sigma_{0xx} & \sigma_{0yx} \\ \sigma_{0xy} & \sigma_{0yy} \end{pmatrix}$.

(ii) Equality of the shear components

P5 Not enforced: $\alpha_{xy} = 0$ in Eq. (10).

(iii) Boundary conditions

P6 Not enforced: $\alpha_{\text{BC}} = 0$ in Eq. (10).

Further, we implement the following variations.

S1 Inverse-Gamma hyperprior distribution: a weakly informative, but proper hyperprior for s^2 and s_0^2 [57].

S2 Student likelihood distribution: admits tails fatter than Gaussian.

S3 Expectation-Maximization algorithm: optimizes a likelihood function that depends on "latent" variables, here s^2 and s_0^2 [69].

Table S1 lists the values of R_σ^2 thus obtained, given the same traction force and stress data sets as for BISM. Values of $1 - R_T^2$ and of χ_T^2 were always very close to 0 and are therefore omitted.

	BISM	$P1$	$P2$	$P3$	$P4$	$P5$	$P6$	$S1$	$S2$
R_σ^2	0.96	0.95	0.96	0.96	0.95	0.75	0.53	0.96	0.96

Table S1: **Robustness to variations of the statistical model.**

	BISM	$N1_-$	$N1_+$	$N2$	$N3$	$N4$	$N5$	$N6$
R_σ^2	0.96	0.99	0.83	0.97	0.91	0.85	0.93	0.96

Table S2: **Robustness to variations of the numerical simulation.**

2.2 Robustness to variations of the numerical simulation

Variations made on the numerical simulations are the following.

- $N1$ Material parameters: keeping $\xi = 10^0 \text{ kPa } \mu\text{m}^{-1}\text{s}$ and $\eta = 10^3 \text{ kPa } \mu\text{m s}$, we vary η' : $\eta' = 10^{-1} \eta$ ($N1_-$); $\eta' = 10^1 \eta$ ($N1_+$).
- $N2$ Elastic rheology: with a Young modulus $E = 10^2 \text{ kPa } \mu\text{m}$ [62, 70], a Poisson ratio $\nu_{2D} = 0.5$ [34]) and a (solid) friction coefficient $\xi_u = 1 \text{ kPa } \mu\text{m}^{-1}$ [71].
- $N3$ No-slip boundary conditions: $\vec{v} = \vec{0}$ at the edge instead of $\sigma \cdot \vec{n} = \vec{0}$, with $\alpha_{BC} = 0$.
- $N4$ Subsystem of a larger tissue: central part of size $R \times C$ of a system of size $3R \times 3C$, with $\alpha_{BC} = 0$, since the boundary conditions on the subsystem are unknown.
- $N5$ Circular geometry: see Fig. S9
- $N6$ Student distribution function of the measurement noise: $St(\nu = 5)$ with unchanged variance s_{exp}^2 .

Table S2 lists the values of R_σ^2 obtained by applying BISM to the traction force field obtained from each of these numerical simulations. We also study the influence of spatial resolution and of the amplitude of measurement noise on the accuracy of inference, see Fig. 4.

2.3 Statistical models

2.3.1 Laplace prior distribution ($P1$)

Since MAP estimation is untractable analytically with a Laplace prior, we use a hierarchical construction [72]. A multivariate Laplace distribution of parameter λ and covariance matrix $2B/\lambda$ is obtained by compounding a Gaussian distribution $\mathcal{N}(\vec{\sigma} \mid \vec{0}, s_0^2 B)$ with an exponential hyperprior for s_0^2 : $H(s_0^2 \mid \lambda) = \frac{\lambda}{2} \exp\left(-\frac{\lambda s_0^2}{2}\right)$, and marginalizing over s_0^2 :

$$\pi_L(\vec{\sigma}) = \int \mathcal{N}(\vec{\sigma} \mid \vec{0}, s_0^2 B) H(s_0^2 \mid \lambda) ds_0^2$$

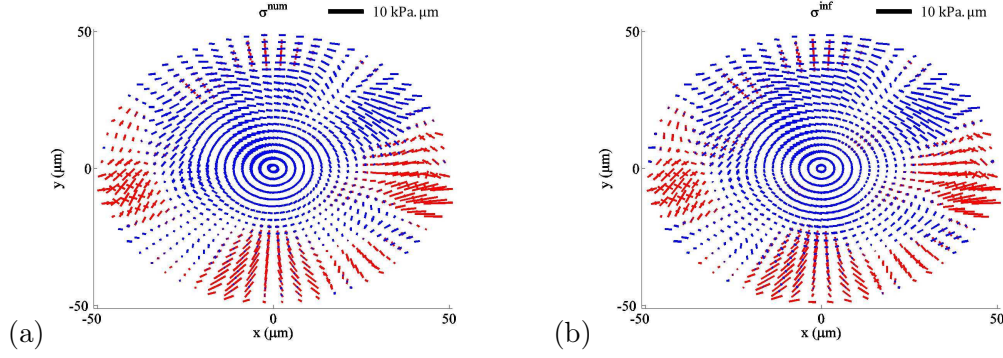


Figure S1: **Polar coordinates.** Monolayer confined to a disc (variation *N5*). Excellent agreement is found between (a) simulated stress σ^{num} and (b) inferred stress σ^{inf} . The stress fields are computed and represented as in Fig. 3, on a 20×60 polar grid in a disc of radius $50 \mu\text{m}$.

Tensor symmetry and boundary conditions are taken into account as above, see Fig. S2a. Using Jeffreys' hyperprior for λ , $H(\lambda) \propto \frac{1}{\lambda}$, MAP estimation leads to the iteration rule

$$s^2_{(k)} = \frac{1}{2N+2} \|\vec{T} - A\vec{\sigma}_{\Pi(k)}\|^2$$

$$\lambda_{(k)} = \frac{2\lambda_{(k-1)}}{4N+2(C+R)} \left(\sqrt{1 + \frac{4\lambda_{(k-1)}}{(4N+2(C+R))^2} \vec{\sigma}_{\Pi(k)}^t B^{-1} \vec{\sigma}_{\Pi(k)} - 1} \right)^{-1}$$

The regularization parameter is defined as

$$\Lambda_L = \frac{1}{2} \lambda l^2 s^2$$

2.3.2 Smoothness prior distribution (*P2*)

We naturally expect the tissue stress field to be a smooth function of space. This information can be embedded in the prior distribution function [46, 42], by penalizing large spatial gradients: (variation *P2*):

$$\pi_s(\vec{\sigma}) \propto \exp \left[-\frac{l^2 \|\vec{\nabla} \vec{\sigma}\|^2 + \alpha_{xy}^2 \|\vec{\sigma}_{xy} - \vec{\sigma}_{yx}\|^2 + \alpha_{BC}^2 \|\vec{\sigma}_{BC}\|^2}{2s_0^2} \right]$$

Discretizing the gradient operator to first order in l leads to a modified effective covariance matrix B_s with $\pi_s(\vec{\sigma}) = \mathcal{N}(\vec{\sigma} \mid \vec{0}, S_{0s} = s_0^2 B_s)$. The iteration rule (19-20) is unchanged.

2.3.3 Inverse-Gamma hyperprior distribution (*S1*)

A natural alternative to the non-informative, improper Jeffreys' distribution for the hyperprior is the weakly informative, proper inverse-Gamma distribution

$$H(s^2 \mid \epsilon, s_H^2) = IG(\epsilon, \epsilon s_H^2) = \frac{(\epsilon s_H^2)^\epsilon}{\Gamma(\epsilon)} \left(\frac{1}{s^2} \right)^{\epsilon+1} \exp \left[-\frac{\epsilon s_H^2}{s^2} \right]$$

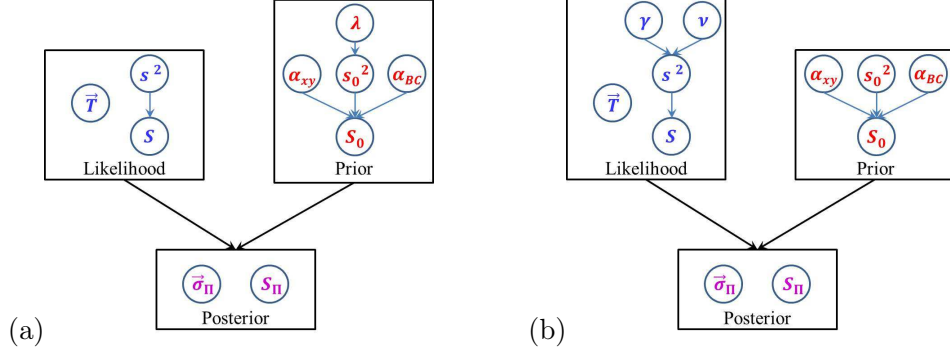


Figure S2: **Schematics of hierarchical Bayesian inversion.** (a) Laplace prior ($P1$). (b) Student likelihood ($S2$).

It tends to Jeffreys' distribution when the parameter ϵ goes to zero, and, conveniently, is conjugate to the Gaussian distribution [57]. Its mode is equal to $\frac{\epsilon}{\epsilon+1} s_H^2$.

For simplicity, we use the same inverse-Gamma hyperprior distribution for s^2 and s_0^2 , and set the additional parameters to constant values $\epsilon = 10^{-1}$, $s_H^2 = 1 \text{ kPa}^2$ and $s_{0H}^2 = 1 \text{ kPa}^2 \mu\text{m}^2$. The evolution equations read (compare with Eqs. (19-20))

$$\begin{aligned} s_{(k)}^2 &= \frac{1}{2N + 2 + 2\epsilon} \left(\|\vec{T} - A\vec{\sigma}_{\Pi(k)}\|^2 + 2\epsilon s_H^2 \right) \\ s_{0(k)}^2 &= \frac{1}{4N + 2(R + C) + 2 + 2\epsilon} \left(\vec{\sigma}_{\Pi(k)}^t B^{-1} \vec{\sigma}_{\Pi(k)} + 2\epsilon s_{0H}^2 \right) \end{aligned}$$

Varying ϵ , the accuracy of inference is excellent as long as $\epsilon < \epsilon_{\max} \approx 3 \cdot 10^{-1}$. Above this value, the bias brought by the finite mean value of s^2 and s_0^2 compromises the inference.

2.3.4 Student likelihood distribution ($S2$)

A simple choice of a zero-mean distribution with tails fatter than Gaussian is the non standardized Student distribution $St(\nu, 0, \gamma)$. It admits a Gaussian limit $St(\nu, 0, \gamma) \rightarrow \mathcal{N}(0, \gamma)$ as $\nu \rightarrow \infty$, and has a finite variance $\frac{\nu\gamma}{\nu-2}$ if $\nu > 2$.

To implement a Student likelihood function in a tractable way, we use again a hierarchical approach [73] (see Fig. S2b). The Student distribution $St(\nu, 0, \gamma)$ is obtained by compounding a Gaussian distribution $\mathcal{N}(\vec{T} | A\vec{\sigma}, s^2 I)$ with an inverse-Gamma distribution $H(s^2 | \gamma, \nu) = IG(\frac{\nu}{2}, \frac{\nu\gamma}{2})$ for the variance s^2 , with Jeffreys' hyperpriors $H(\gamma) \propto \frac{1}{\gamma}$, $H(\nu) \propto 1$ for γ and ν , and by integrating over s^2

$$L_S(\vec{T} | \vec{\sigma}) = \int \mathcal{N}(\vec{T} | A\vec{\sigma}, s^2 I) H(s^2 | \gamma, \nu) H(\gamma) H(\nu) ds^2$$

The iteration rule reads

$$\begin{aligned}
s_{0(k)}^2 &= \frac{1}{4N + 2(R + C) + 2} \vec{\sigma}_{\Pi(k)}^t B^{-1} \vec{\sigma}_{\Pi(k)} \\
\gamma_{(k)} &= \frac{\nu_{(k-1)} - 2}{\nu_{(k-1)}} \frac{1}{2N + \nu_{(k-1)} + 2} \left(\|\vec{T} - A\vec{\sigma}_{\Pi(k)}\|^2 + \nu_{(k-1)}\gamma_{(k-1)} \right) \\
\psi\left(\frac{\nu_{(k)}}{2}\right) - \log\left(\frac{\nu_{(k)}}{2}\right) &= \log\left(\frac{\nu_{(k-1)} - 2}{\nu_{(k-1)}}\right) - \frac{\nu_{(k-1)} - 2}{\nu_{(k-1)}} + 1
\end{aligned}$$

where ψ is the digamma function, and the last equation is solved for $\nu_{(k)}$. The regularization parameter is defined as

$$\Lambda_S = \frac{l^2 \gamma}{s_0^2} \frac{\nu}{\nu - 2}$$

2.3.5 Expectation-maximization algorithm ($S\mathcal{J}$)

A classical alternative to MAP optimization is the expectation-maximization (EM) algorithm [69]. Once $\vec{\sigma}_{\Pi(k)}$ is computed using the $(k-1)$ th parameter values $s_{(k-1)}^2$ and $s_{0(k-1)}^2$, we need to

E step: define a function Q as the expectation value over $\vec{\sigma}$ of the log-posterior

$$Q(s^2, s_0^2 \mid s_{(k-1)}^2, s_{0(k-1)}^2, \vec{\sigma}_{\Pi(k)}) = E_{\vec{\sigma}} \left[\log \Pi \left(\vec{\sigma}, s^2, s_0^2 \mid \vec{T}, s_{(k-1)}^2, s_{0(k-1)}^2, \vec{\sigma}_{\Pi(k)} \right) \right]$$

M step: optimize this function Q over respectively s^2 and s_0^2 to calculate the k th parameter values $s_{(k)}^2$ and $s_{0(k)}^2$

$$\begin{aligned}
s_{(k)}^2 &= \operatorname{argmax}_{s^2} Q(s^2, s_0^2 \mid s_{(k-1)}^2, s_{0(k-1)}^2, \vec{\sigma}_{\Pi(k)}) \\
s_{0(k)}^2 &= \operatorname{argmax}_{s_0^2} Q(s^2, s_0^2 \mid s_{(k-1)}^2, s_{0(k-1)}^2, \vec{\sigma}_{\Pi(k)})
\end{aligned}$$

We obtain the iteration rule [74] (compare with Eqs. (19-20))

$$\begin{aligned}
s_{(k)}^2 &= \frac{1}{2N + 2} \left(\|\vec{T} - A\vec{\sigma}_{\Pi(k)}\|^2 + s_{(k-1)}^2 \left(4N + 2(R + C) - \frac{\operatorname{tr} S_{\Pi}}{s_{0(k-1)}^2} \right) \right) \\
s_{0(k)}^2 &= \frac{1}{4N + 2(R + C) + 2} \left(\vec{\sigma}_{\Pi(k)}^t B^{-1} \vec{\sigma}_{\Pi(k)} + \operatorname{tr} S_{\Pi} \right)
\end{aligned}$$

Convergence is fast, similar to MAP estimation, but the calculation is more demanding computationally due to the need to evaluate S_{Π} at each step.

3 Parameter and hyperparameter optimization

3.1 Convergence

In *Validation: numerical data*, we infer the stress field of a viscous tissue with BISM. For initial values $s_{(0)}^2 = 10^{-1} \text{ kPa}^2$ and $s_{0(0)}^2 = 10^2 \text{ kPa}^2 \mu\text{m}^2$, the iterative resolution

	BISM	$P1$	$P2$	$P3$	$P4$	$P5$	$P6$	$S1$	$S2$
$\Lambda_{(\infty)}$	$5.5 \cdot 10^{-6}$	$8.1 \cdot 10^{-4}$	$1.2 \cdot 10^{-4}$	$3.7 \cdot 10^{-6}$	$1.1 \cdot 10^{-5}$	$8.8 \cdot 10^{-6}$	$2.3 \cdot 10^{-3}$	$5.6 \cdot 10^{-4}$	$1.2 \cdot 10^{-5}$

	BISM	$N1_-$	$N1_+$	$N2$	$N3$	$N4$	$N5$	$N6$
$\Lambda_{(\infty)}$	$5.5 \cdot 10^{-6}$	$1.7 \cdot 10^{-6}$	$5.6 \cdot 10^{-6}$	$3.9 \cdot 10^{-6}$	$1.9 \cdot 10^{-3}$	$6.2 \cdot 10^{-3}$	$2.6 \cdot 10^{-5}$	$5.6 \cdot 10^{-5}$

Table S3: **Optimal values** $\Lambda_{(\infty)} = l^2 s_{(\infty)}^2 / s_{0(\infty)}^2$ of the regularization parameter for all statistical models and numerical simulations studied in *Results*.

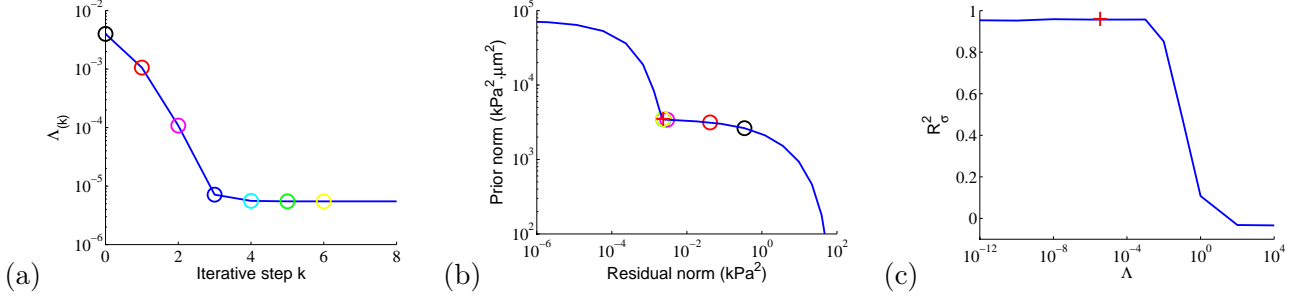


Figure S3: **Convergence: BISM.** (a) $\Lambda_{(k)} = l^2 s_{(k)}^2 / s_{0(k)}^2$ vs. iterative step k in semilogarithmic scale. (b) L-curve: effective prior norm $\vec{\sigma}_{\Pi}^t B^{-1} \vec{\sigma}_{\Pi}$ vs. residual norm $\|\vec{T} - A\vec{\sigma}_{\Pi}\|^2$ in logarithmic scale. The colored circles correspond to the successive steps depicted in (a). Black circle: initial condition; crossed circle: asymptotic value, step $k = 6$. The asymptotic value reached by the iterative method sits at the apex of the L-curve. (c) Coefficient of determination R_{σ}^2 vs. Λ in semilogarithmic scale. Red cross: asymptotic value $\Lambda_{(\infty)} = 5.5 \cdot 10^{-6}$.

method converges in a few steps towards an optimal value of the regularization parameter $\Lambda_{(\infty)} = 5.5 \cdot 10^{-6}$ ($s_{(\infty)}^2 = 4.7 \cdot 10^{-7} \text{ kPa}^2$, $s_{0(\infty)}^2 = 3.4 \cdot 10^{-1} \text{ kPa}^2 \mu\text{m}^2$), see Fig. S3a

When performing Tikhonov regularization, the optimal regularization parameter is located at the apex of the L-curve [75]. Here, the L-curve is a parametric plot of the prior norm $\vec{\sigma}_{\Pi}^t B^{-1} \vec{\sigma}_{\Pi}$ vs. the residual norm $\|\vec{T} - A\vec{\sigma}_{\Pi}\|^2$ as Λ varies, see Fig. S3b. Superposing on the L-curve the points obtained by iteration, we find excellent agreement between the two methods. MAP estimation is more economical computationally since only a few points are needed to determine the optimal parameters. Successive iterations displace the representative circles towards smaller values of the residual norm along the L-curve. In order to obtain convergence, we need to start from initial conditions located on the right hand side of the apex. The representative circle runs away towards unphysically small values of Λ when starting from initial conditions located on the left hand side of the apex. Another advantage of MAP estimation is to determine self-consistently the values of s^2 and s_0^2 , needed to compute S_{Π} and the error bars $\delta\vec{\sigma}$.

The value $\Lambda_{(\infty)} = 5.5 \cdot 10^{-6} \ll 1$ gives more importance to the likelihood than to the prior. Inferring the stress field at fixed values of s_0^2 and s^2 , we plot the coefficient of determination R_{σ}^2 vs. Λ (Fig. S3c) and find that the accuracy of inference is excellent as

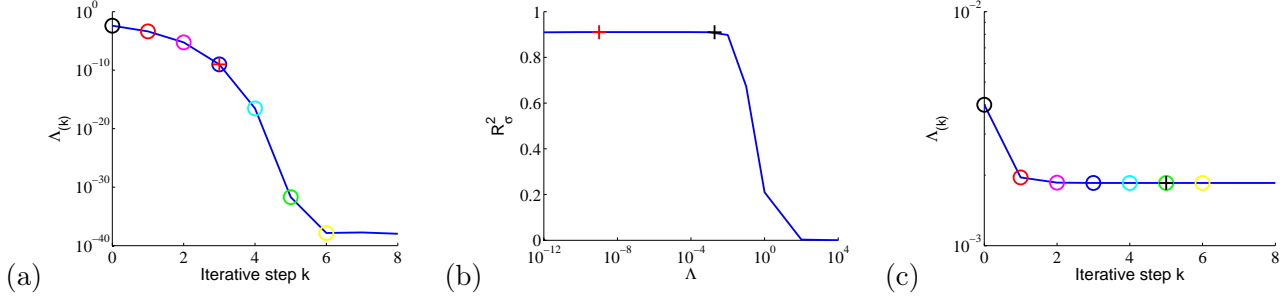


Figure S4: **Convergence: $N3$.** (a) $\Lambda_k = l^2 s_{(k)}^2 / s_0^2$ vs. iterative step k in semilogarithmic scale. Red cross: $k = 3$, $\Lambda = 1.0 \cdot 10^{-9}$, see text. (b) Coefficient of determination R_σ^2 vs. Λ . The red and black crosses locate the asymptotic values found in (a) and (c). (c) Λ_k vs. iterative step k in semilogarithmic scale at constant $s^2 = 10^{-3} \text{ kPa}^2$, with $\Lambda_{(\infty)} = 1.9 \cdot 10^{-3}$. The black and colored circles in (a) and (c) correspond respectively to the initial condition and to successive iterative steps

soon as $\Lambda < 10^{-3}$, and that further decreasing Λ no longer improves accuracy. BISM is robust against variations of the ratio s^2/s_0^2 provided that the weight given to information contained in the prior is small enough.

This pattern describes faithfully the convergence of the resolution method for most of the statistical models and numerical data sets we investigated: convergence occurs within a few steps towards optimal values of the regularization parameter in the range $[10^{-6}, 10^{-3}]$, see Table S3.

Variations $P6$, $N3$ and $N4$, which correspond to changes related to boundary conditions, differ in the following way. The resolution method converges fast, but to an unphysically small value of $\Lambda_{(\infty)}$ (of the order of 10^{-38} for $N3$, see Fig. S4a). Since the coefficient of determination still plateaus close to 1 when $\Lambda < 10^{-2}$ (Fig. S4b), selecting an early step (typically $k = 3$) for inference works well, and gives the value $\Lambda_{(\infty)} = 1.0 \cdot 10^{-9}$.

However, setting s^2 to a constant value and ignoring Eq. (19) allows to self-consistently determine s_0^2 iteratively using Eq. (20) only. When dealing with experimental data, a natural estimate of s is the experimental error bar on traction force data. For the numerical data sets $P6$, $N3$ and $N4$, we use $s^2 = 10^{-3} \text{ kPa}^2 \approx s_{\text{exp}}^2$, the noise amplitude (see Table S3). For $N3$, iterations over $\vec{\sigma}_{\Pi(k)}$ and $s_{0(k)}^2$ exhibit rapid convergence towards $\Lambda_{(\infty)} = 1.9 \cdot 10^{-3}$ (see Fig. S4c), on the plateau of the $R_\sigma^2(\Lambda)$ curve. In this case, error bars $\delta\hat{\sigma}$ on the inferred stress are less meaningful since they depend on the numerical value used for s^2 . Of course if s^2 is fixed by the experiment then error bars are more reliable. Due to the large plateau of the $R_\sigma^2(\Lambda)$ curve, both parameter determination methods yield the same results.

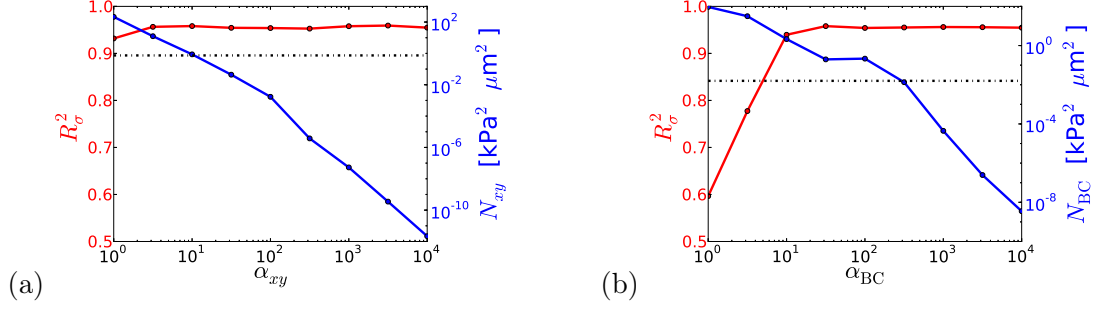


Figure S5: **Hyperparameters α_{xy} and α_{BC} : BISM.** (a) R_σ^2 (red) and N_{xy} (blue) vs. α_{xy} . (b) R_σ^2 (red) and N_{BC} (blue) vs. α_{BC} . On both graphs, the black dashed line gives the reference values, $N_{xy}^{\text{num}} = 7.4 \times 10^{-1} \text{ kPa}^2 \mu\text{m}^2$ and $N_{BC}^{\text{num}} = 1.6 \times 10^{-2} \text{ kPa}^2 \mu\text{m}^2$ computed for the numerical data set.

3.2 Hyperparameters α_{xy} and α_{BC}

In principle the values of α_{xy} and α_{BC} could also be determined self-consistently. For simplicity, we set these hyperparameters to constant, large values.

In order to determine which hyperparameter values will ensure that stress tensor symmetry and boundary conditions are respected, we perform BISM on the *Viscous* data set for a large range $[1, 10^4]$ of fixed values of α_{xy} and α_{BC} . In addition to R_σ^2 , we define the partial prior norms $N_{xy} = \|\vec{\sigma}_{xy} - \vec{\sigma}_{yx}\|^2$ and $N_{BC} = \|\vec{\sigma}_{BC}\|^2$ as specific measures of accuracy. Fig. S5a shows how R_σ^2 and N_{xy} vary as a function of α_{xy} . The partial prior norm N_{xy} decreases with α_{xy} . Above $\alpha_{xy} \simeq 10$, N_{xy} becomes smaller than the reference value N_{xy}^{num} computed on the (noisy) data set. Since the global measure R_σ^2 plateaus for $\alpha_{xy} > 10^1$, values of α_{xy} larger than 10^1 ensure equality of the shear stress components. Note that as α_{xy} decreases, R_σ^2 decreases towards the limit $R_\sigma^2(\alpha_{xy} = 0) = 0.75$ found for variation *P5*. The same reasoning applies to α_{BC} , for which R_σ^2 plateaus for $\alpha_{xy} > 3 \times 10^1$, and the reference value N_{BC}^{num} computed on the noisy data set is crossed above 300, see Fig. S5b.

In practice, we use the conservative values $\alpha_{xy} = 10^3$ and $\alpha_{BC} = 10^3$ for all statistical models and data sets.

4 Supplementary figures

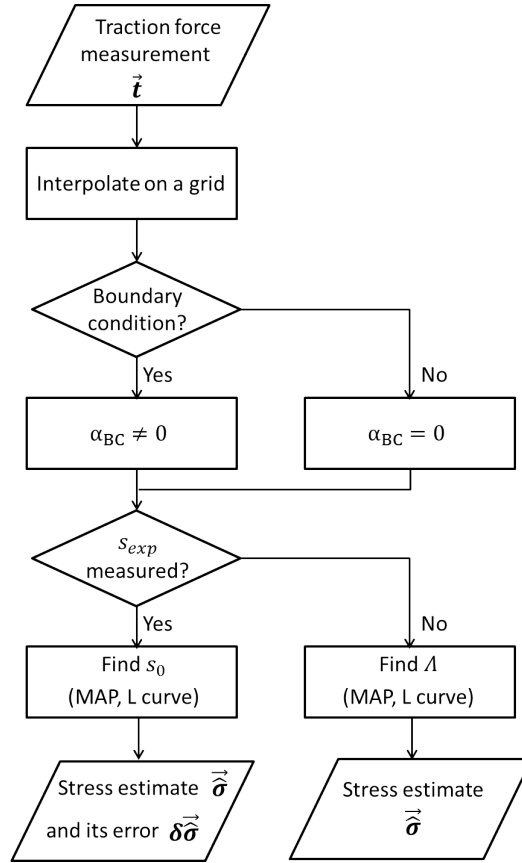


Figure S6: **Flowchart of the algorithm.**

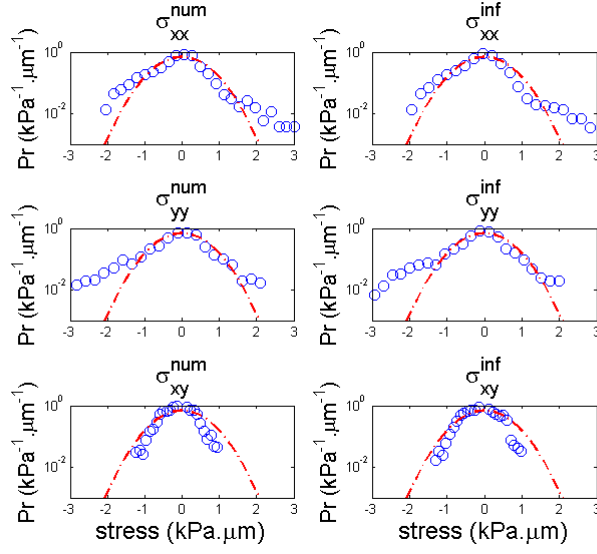


Figure S7: **Stress probability distribution functions.** We compare the distributions (blue circles) of simulated (left column) and inferred (right column) stresses, for each component, in the *Viscous* case. The red dashed line corresponds to the Gaussian prior distribution function with a standard deviation $s_0 = 0.57 \text{ kPa} \cdot \mu\text{m}$.

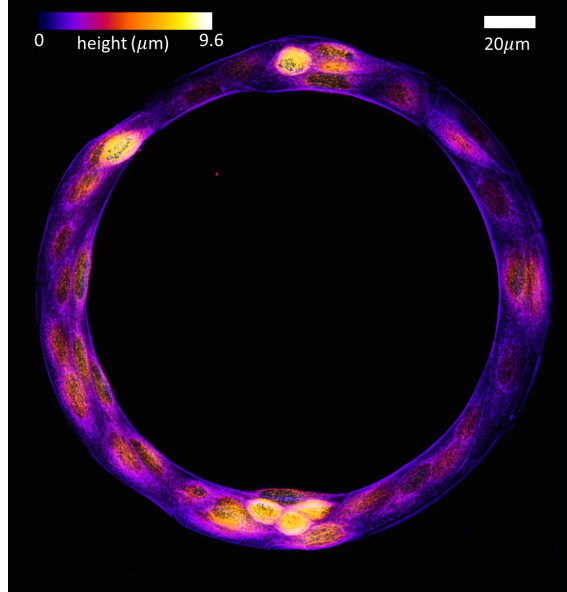
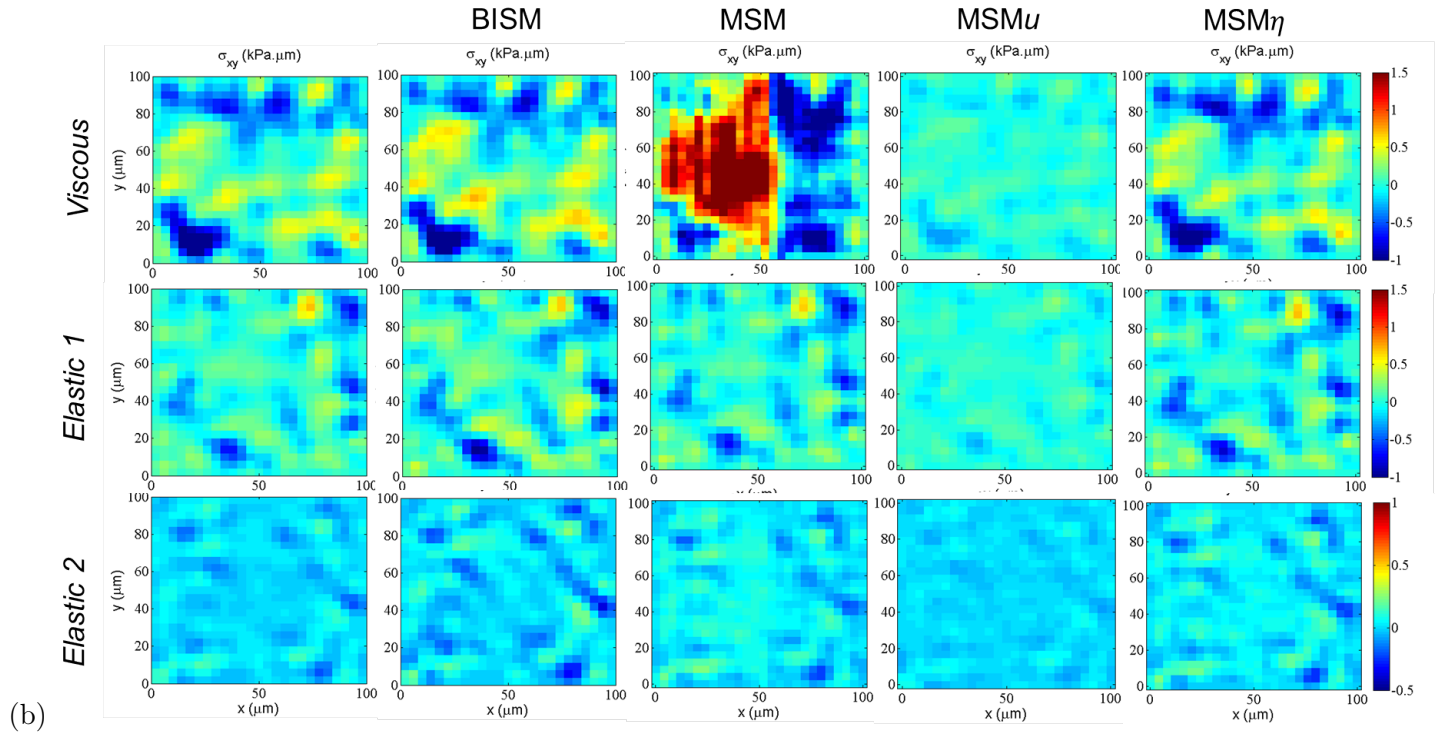
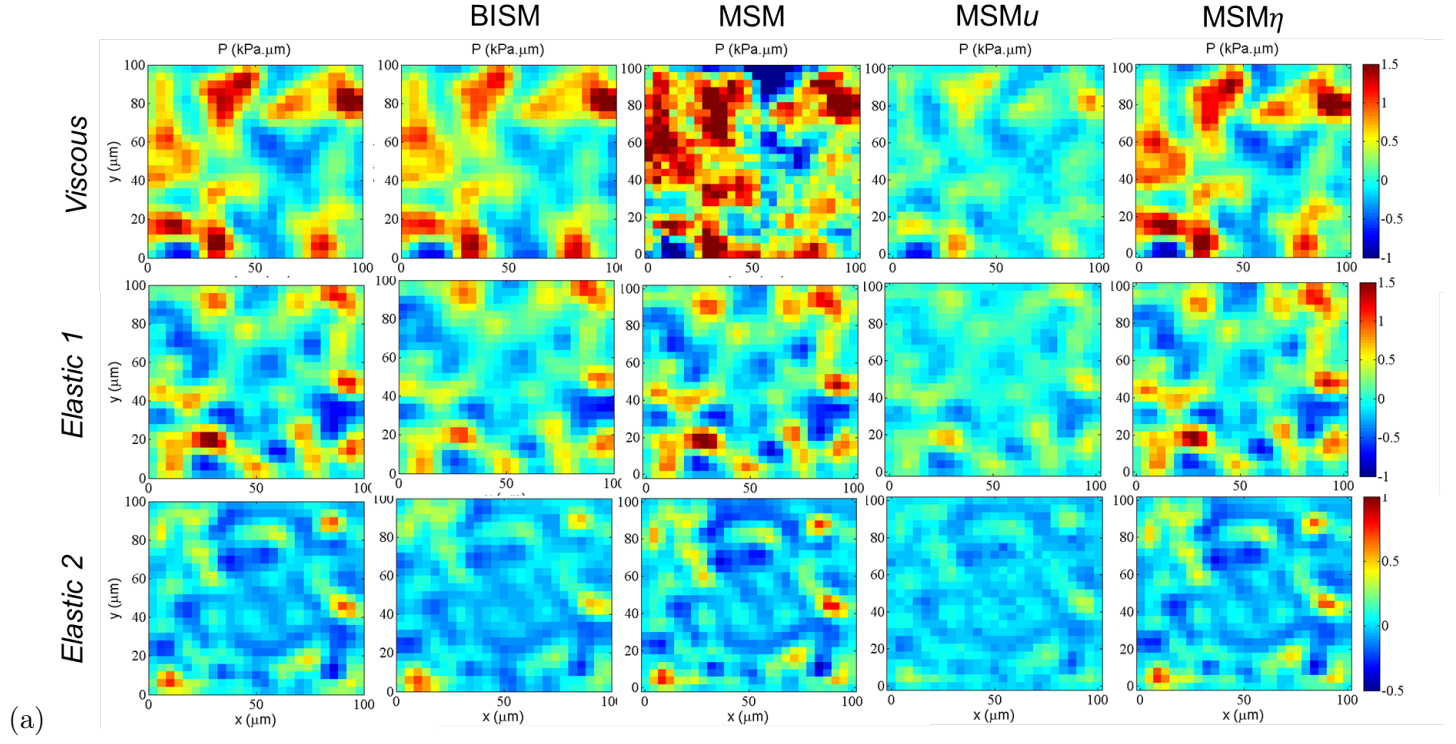


Figure S8: **Height variation of the annular cell monolayer.** Z-stack measurement: each color corresponds to a height bin in the z direction with a resolution of $0.4 \mu\text{m}$. Scale bar: $20 \mu\text{m}$.



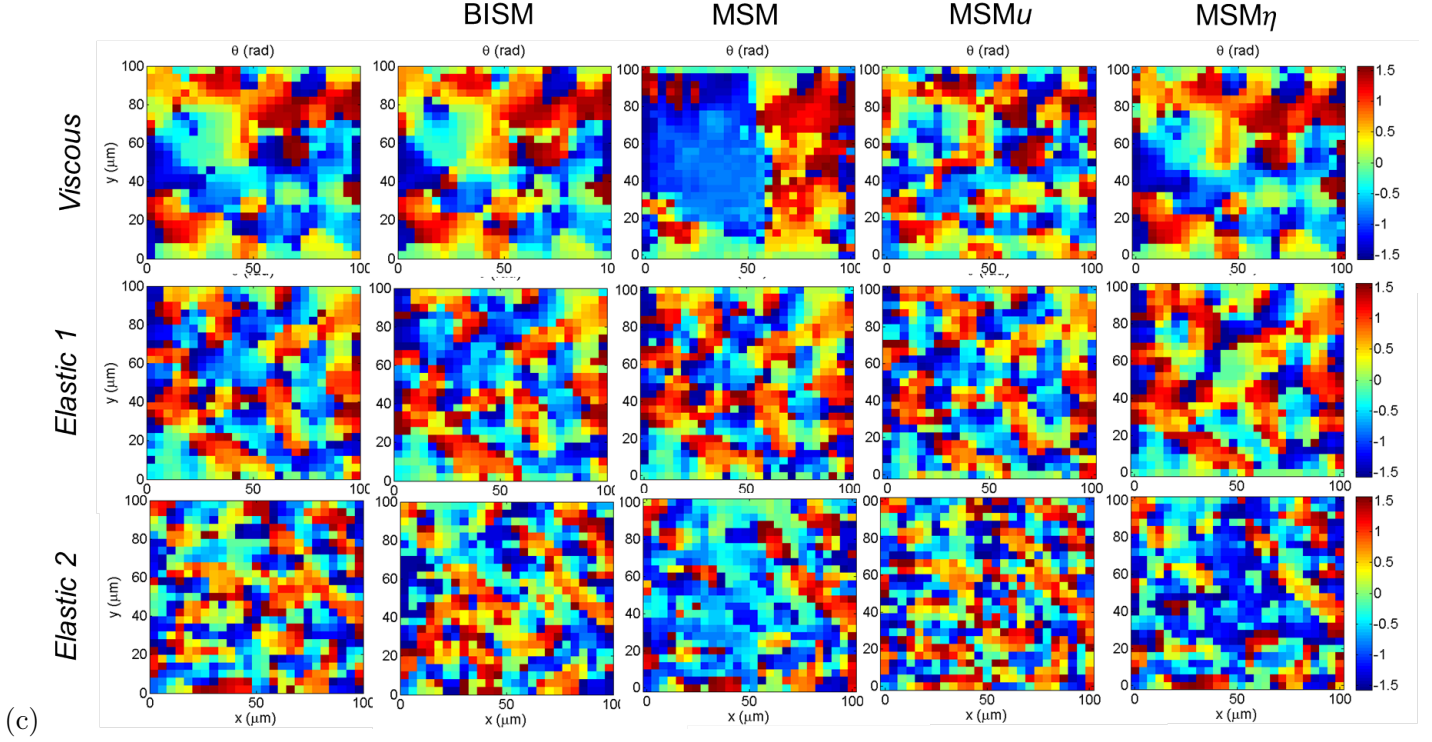


Figure S9: **Comparison between BISM and monolayer stress microscopies.** Numerical data (first column) for: (a) pressure; (b) shear stress; (c) stress orientation (angle θ between the principal stress eigenvector and the x axis, $\theta \in [-\pi/2, \pi/2]$) are compared with inferred data obtained with BISM, MSM, MSM u and MSM η (see text for definitions, spatial resolution: $4 \mu\text{m}$). Traction force data sets were obtained with material parameter values $\eta = 10^3 \text{ kPa } \mu\text{m s}$, $\eta' = \eta$ (*Viscous*); $E = 10^2 \text{ kPa } \mu\text{m}$, $\nu_{2D} = 0.5$ [26] (*Elastic 1*), $E = 10 \text{ kPa } \mu\text{m}$, $\nu_{2D} = 0.5$ [36] (*Elastic 2*). A white noise of relative amplitude 5 % is added in all cases.